# FABRICATION AND CHARACTERIZATION

# OF PLANAR HALL DEVICES

**MAY THU WIN**

**(B.Eng) Yangon Technological University**

**A THESIS IS SUBMITTED**

**FOR THE DEGREE OF MASTER OF ENGINEERING**

**DEPARTMENT OF ELECTRICAL AND COMPUTER ENGINEERING**

**NATIONAL UNIVERSITY OF SINGAPORE**

**2003**

# ACKNOWLEDGEMENT

The author wishes to express her most sincere gratitude to her supervisor, Dr Adekunle Olusola Adeyeye for his encouragement, understanding, motivation, guidance and concern throughout the course of her M. Eng research work. His knowledge and experience has definitely made this project a success. She also would like to thank to Dr. Vivian Ng for her kind support, advice and encouragement.

She would also like to thank the following staffs for their help rendered throughout this project: Mr. Walter Lim (Microelectronics Lab.), Ms Loh Fong Leong and Miss Liu Ling (Information Storage Materials Lab), Mrs. Ho Chiow Moo (Centre for Integrated Circuits Failure Analysis Research Lab) and Mrs. Ah Lian Kiat (MOS Device Lab). Without their help, the project would not be possible.

She is also very grateful to her laboratory mates from Information Storage Materials Lab – Aung Kyaw Oo, Lim Zhao Lin, Chen Fang Hao, Zhao Zhiya, Muhammad Khaled Husain, Zhao Qiang, Fong Kien Hoong, Guo Jie, Maung Kyaw Min Tun, Wang Chen Chen, Shikha Jain and Verma, Lalit Kumar for their support and companionship.

Most of all she would like to thank her beloved parents and sisters, her uncle's family for their love, undying support, financial assistance and her friends for their continuous encouragement throughout this whole project.

Last but not the least; she would like to thank all those who have contributed to this project in one way or another.

## TABLE OF CONTENTS

**ACKNOWLEDGEMENTS** **i**

**TABLE OF CONTENTS** **ii**

**SUMMARY** **v**

**MAJOR SYMBOLS AND ABBREVIATION** **vii**

**LIST OF FIGURES** **ix**

**LIST OF TABLES** **xii**

**LIST OF PUBLICATIONS** **xiii**

**CHAPTER 1: INTRODUCTION** **1**

1.1 Background 1

1.2 Objectives 3

1.3 Organization of Thesis 3

**CHAPTER 2: THEORY** **5**

2.1 Magnetoresistance Effect (MR) 5

2.2 Anisotropic Magnetoresistance Effect (AMR) 6

2.3 Giant Magnetoresistance Effect (GMR) 8

2.4 Planar Hall Effect (PHE) 11

2.5 Interlayer Exchange Coupling 14

**CHAPTER 3: EXPERIMENTAL TECHNIQUES** **19**

3.1 Fabrication of Planar Hall Devices by Using Shadow Mask 19

3.1.1: Layout of Masks 19

3.1.2: Steps for shadow mask technique 20

3.1.3: Cleaning of silicon wafers 21

3.1.4: Sputtering 22

3.1.5: Fabrication Procedure for Shadow Mask Technique 24

3.1.6: Wire Bonding 25

3.2 Fabrication of Planar Hall Devices by Using Photolithography Process 27

3.2.1: Masks 27

3.2.2: Photolithography Process 29

3.2.3: Evaporation 36

3.2.4: Lift off 39

3.2.5: Sputtering and Wire Bonding 39

3.3 Characterization Techniques 40

3.3.1: Four Point Probe Method 40

3.3.2: Vibrating Sample Magnetometer (VSM) 41

**CHAPTER 4: INTERLAYER EXCHANGE COUPLING IN MAGNETIC MULTILAYER FILMS** **44**

4.1 Overview 44

4.2 Introduction 44

4.3 Fabrication Procedure 45

4.4 Magnetization reversal in [Co (10 nm)/Cu ($t_{Cu}$) /Co (10 nm)]$_2$ multilayer films 47

4.5 Magnetotransport in Co / Cu/ Co Multilayer films 53

4.5.1: Comparison of PHE and MR as a Function of Field Orientation 59

4.5.2: PHE voltages as a function of orientation of applied field 60

4.5.3: AMR voltages as a function of orientation of applied field 62

4.6 PHE and AMR effects in [NiFe (10nm)/ Cu ($t_{Cu}$)/ NiFe (10nm)]$_2$ Multilayer 64

4.7 Summary 66

**CHAPTER 5: FINITE SIZE EFFECTS OF MAGNETO TRANSPORT PROPERTIES IN MULTILAYER STRUCTURES 68**

5.1 Overview 68

5.2 Experimental Procedure and Measurement Set up 68

5.3 Theory 69

5.4 Results and Analysis 70

5.4.1: Experimental Results and Analysis for [Co (10 nm)/ Cu ($t_{Cu}$) / Co (10 nm)]$_2$ Multilayer Structures 70

5.4.2: Field Orientations effect on PHE and AMR results 75

5.4.3: Experimental Results and Analysis for [NiFe (10nm)/ Cu ($t_{Cu}$)/ NiFe 10 nm)]$_2$ Multilayer Structure 79

5.5 Devices fabricated using E - beam Lithography method 84

5.6 Summary 86

**CHAPTER 6: CONCLUSION AND FUTURE RECOMMENDATIONS 88**

6.1 Conclusion 88

6.2 Future Recommendations 89

# SUMMARY

The oscillatory interlayer exchange coupling between two ferromagnetic layers through spacer layers has recently been extensively investigated due to both fundamental interest in the physics of giant magnetoresistance (GMR) and applied interest associated with the development of novel magnetic sensors and non-volatile memory arrays. In this project, the effect of multilayer exchange coupling in magnetic multilayers has been investigated using a combination of anisotropic magnetoresistance (AMR) and planar Hall Effect (PHE) measurements. These devices were fabricated using shadow mask technique. We have studied the magnetic properties of [Co (10nm)/ Cu ($t_{Cu}$)/ Co (10 nm)]$_2$ and [NiFe (10 nm)/ Cu($t_{Cu}$)/ NiFe (10 nm)]$_2$ multilayer films as a function of Cu spacer layer thickness using Vibrating Sample Magnetometer (VSM). We observed a transition from ferromagnetic to antiferromagnetic coupling as the thickness of spacer layer was varied from 0 to 10nm. From our measurements, we found that when the copper spacer layer thickness is less than 2nm, ferromagnetic coupling is favored. However, when copper thickness is greater than 2nm, antiferromagnetic coupling dominates. The shape and detailed features of the M – H loops is strongly dependent on the Cu spacer layer thickness.

In another experiment, the role of finite size on the magnetic properties of multilayer films and the interlayer exchange coupling were investigated. Devices with different widths were fabricated using optical lithography technique, electron beam evaporation and lift off method. The effect of device finite size on the PHE and AMR output is investigated. We observed a size dependent effect due to the demagnetizing field.

We conclude that planar Hall Effect (PHE) is a powerful probe of interlayer exchange coupling in magnetic multilayer.

# LIST OF TABLES


| | | |
|---|---|---|
| Table 3.1 | Sputter parameters for Co/Cu multilayer structure | 24 |
| Table 3.2 | Sputter parameters for Al bond pads | 25 |
| Table 3.3 | Wire bonding parameters | 26 |
| Table 3.4 | Dimensions for the planar hall device mask | 28 |
| Table 3.5 | The chemical and physical properties of AZ 7220 photoresist series | 31 |
| Table 3.6 | The summary for the materials used in this fabrication and properties | 39 |
| Table 5.1 | The parameters for the deposition of Co, Cu, Al and NiFe materials | 71 |
| Table 5.2 | Compilation of AMR measurement for the field perpendicular to current direction | 76 |

# LIST OF FIGURES


| | | |
|---|---|---|
| Fig. 2.1 | Electrical resistance anisotropy between the parallel and normal directions of magnetization | 6 |
| Fig. 2.2 | (a) Schematic diagram of AMR configuration<br>(b) Graph for AMR vs angle θ | 7 |
| Fig. 2.3 | Schematic diagram of spin state in GMR structure | 9 |
| Fig. 2.4 | (a) Schematic illustration showing electrical connections for PHE measurement<br>(b) Typical PHE output as a function of field orientation | 11 |
| Fig. 2.5 | FM layers with magnetic order correlated by the (a) FM and (b) AFM exchange coupling | 15 |
| Fig. 3.1 | Mask used for deposition of materials for planar hall device | 19 |
| Fig. 3.2 | Mask used for deposition of contact pads for device | 20 |
| Fig 3.3 | Schematic diagram of the device after aligning | 20 |
| Fig. 3.4 | Steps for fabrication of devices by shadow mask technique | 21 |
| Fig. 3.5 | Schematic diagram of the sputtering process | 22 |
| Fig. 3.6 | Cryo Vac thin film Deposition System | 23 |
| Fig. 3.7 | Photo of the spin coater | 25 |
| Fig 3.8 | Photo of Wire Bonder (4523 AD) | 26 |
| Fig. 3.9 | Mask for the first layer of planar hall devices | 27 |
| Fig. 3.10 | Basic sketch for the device | 28 |
| Fig. 3.11 | Mask for the second layer of contact pads | 29 |
| Fig. 3.12 | Schematic diagram of photolithography process | 30 |
| Fig. 3.13 | Photo of Mask Aligner (MA6) | 32 |
| Fig. 3.14 | Steps for device fabrication using lithography process | 33 |
| Fig. 3.15 | Fabrication steps using photolithography process | 34 |
| Fig. 3.16 | Picture of Evaporator System (EV 2000) | 37 |

| | | |
|---|---|---|
| Fig. 3.17 | Magnetotransport measurement set up system | 40 |
| Fig. 3.18 | Schematic Diagram of Vibrating Sample Magnetometer (VSM) | 42 |
| Fig. 4.1 | Layer structure of the Co/Cu/Co multilayer | 47 |
| Fig. 4.2 | Magnetic Hysteresis loops for different Cu spacer layer thickness in [Co/Cu ($t_{Cu}$)/ Co]$_2$ multilayer structure | 49 |
| Fig. 4.3 | Detailed [Co/Cu ($t_{Cu}$)/ Co]$_2$ structure for (a) $t_{Cu} = 0$ and (b) $t_{Cu} = 2$ nm (c) $t_{Cu} = 5$ nm in [Co/Cu ($t_{Cu}$)/ Co]$_2$ structure | 50 |
| Fig. 4.4 | The value of (a) coercivity ($H_c$), (b) saturation field ($H_s$) and (c) squareness as a function of Cu spacer layer thickness in [Co (10 nm)/Cu ($t_{Cu}$)/Co (10 nm)]$_2$ multilayer structure | 52 |
| Fig. 4.5 | Electrical connections for AMR and PHE measurements | 54 |
| Fig. 4.6 | Planar Hall Effect (V35 – H) and AMR ($V_{23}$ – H) as a function of Cu spacer layer thickness for field applied along $\theta = 0°$ | 56 |
| Fig. 4.7 | PHE ($V_{35}$ – H) and AMR ($V_{23}$ – H) as a function of Cu spacer layer thickness for field applied along $\theta = 90°$ | 58 |
| Fig. 4.8 | Direct comparison of PHE and MR output voltage for [Co (10nm) /Cu (5nm)/Co (10nm)]$_2$ multilayer | 60 |
| Fig. 4.9 | PHE voltages as a function of applied field relative to the direction of the sense current for [Co/$Cu_t$/Co]$_2$ multilayer as a function of Cu thickness | 62 |
| Fig. 4.10 | AMR output voltage ($V_{23}$) as a function of field orientation relative to the direction of sense current in [Co/$Cu_t$/ Co] multilayer structure for various $t_{Cu}$ | 64 |
| Fig. 4.11 | Comparison of PHE and MR results as a function of Cu spacer layer thickness in [NiFe (10nm)/ Cu ($t_{Cu}$)/ NiFe (10 nm)]$_2$ structure for 90° field orientation | 66 |
| Fig. 4.12 | PHE and AMR output voltages for [NiFe (10 nm)/ Cu (5 nm)/ NiFe (10nm)]$_2$ multilayer structure with different field Orientations | 67 |
| Fig. 5.1 | Schematic representation of the device geometry with external Contacts | 71 |
| Fig. 5.2 | PHE results as a function of different widths in [Co (10nm)/ Cu (5 nm)/ Co (10 nm)]$_2$ multilayer structures | 74 |

| | | |
|---|---|---|
| Fig. 5.3 | Comparison of AMR output voltages for different size widths in [Co (10nm)/ Cu (5 nm)/ Co (10 nm)]$_2$ multilayer structure | 75 |
| Fig. 5.4 | PHE output as a function of Cu spacer layer thickness for [Co (10 nm)/Cu ($t_{Cu}$)/ Co (10 nm)]$_2$ multilayer films with device width = 20 μm | 77 |
| Fig. 5.5 | Comparison of AMR output voltages for different Cu spacer layer thickness for [Co (10nm)/ Cu (5 nm)/ Co (10 nm)]$_2$ multilayer structure with device width 20μm | 78 |
| Fig. 5.6 | PHE and AMR output voltages as a function of the orientation of applied field relative to the current direction | 79 |
| Fig. 5.7 | Hysteresis loops as a function of Cu spacer layer thickness in [Co (10 nm)/ Cu ($t_{Cu}$) / Co (10 nm)]$_2$ multilayer structures | 81 |
| Fig. 5.8 | PHE and AMR output voltages for [NiFe (10nm)/ Cu ($t_{Cu}$)/ NiFe 10 nm)]$_2$ multilayer structure as a function of Cu spacer layer thickness when the applied field is perpendicular to the sense current direction | 83 |
| Fig. 5.9 | Hysteresis loops as a function of Cu spacer layer thickness in [NiFe (10 nm)/ Cu ($t_{Cu}$)/ NiFe (10 nm)]$_2$ multilayer structure | 85 |
| Fig. 5.10 | The value of (a) coercivity ($H_c$), (b) saturation field ($H_s$) and (c) squareness as a function of Cu spacer layer thickness in [NiFe (10 nm)/Cu ($t_{Cu}$)/NiFe (10 nm)]$_2$ multilayer structure | 87 |
| Fig. 5.11 | Comparison of PHE and AMR output voltages for device width w = 1 μm | 88 |
| Fig. 5.12 | Comparison of PHE and AMR output voltages for devices width w = 500 nm | 89 |

# MAJOR SYMBOLS AND ABBREVIATION

| | |
|---|---|
| Å | Angstroms ($10^{-10}$ m) |
| AFM | Antiferromagnetic Coupling |
| Ag | Silver |
| Al | Aluminum |
| AMR | Anisotropic Magnetoresistance |
| Co | Cobalt |
| Cr | Chromium |
| Cu | Copper |
| DC | Direct Current |
| DI | De- Ionized water |
| FM | Ferromagnetic Coupling |
| gm | gram |
| GMR | Giant Magnetoresistance |
| $H_c$ | Coercivity |
| $H_s$ | Saturation Field |
| I | Current |
| IPA | Isopropanol |
| M | Magnetization |
| $M_r$ | Remanent magnetization |
| ML | Multilayer |
| MR | Magnetoresistance |
| NiFe | Permalloy |
| PHE | Planar Hall Effect |

| | |
|---|---|
| Ru | Ruthenium |
| s | Second (time) |
| S | Squareness |
| $S^*$ | Squareness ratio |
| Ta | Tantalum |
| V | Voltage |
| Vs | versus |
| VSM | Vibrating Sample Magnetometer |
| W | Watt |

# Chapter 1

# Introduction

## 1.1 Background

Metallic multilayered thin films in which ferromagnetic (F) and nonferromagnetic metallic layers (N) alternate, have attracted considerable attention due to their unique physical properties and potential for technological application. Many magnetic multilayer systems exhibit a coupling between the magnetic layers mediated by the non-magnetic spacers, which oscillates periodically between ferromagnetic (FM) and antiferromagnetic (AFM) as the spacer-layer thickness varies in the range of 0.5-5nm [1-4]. The oscillatory interlayer exchange coupling between two ferromagnetic layers through spacer layers has recently been extensively investigated due to both fundamental interest in the physics of giant magnetoresistance (GMR) and applied interest associated with the development of novel magnetic sensors and non-volatile memory arrays [5].

Magnetic sensors have been used in one form or another for many hundreds of years [6]. The magnetoresistive effect is a widely used magnetic phenomenon having applications in various technical areas. The most important field for magnetoresistive sensors is the high density data storage systems in view of increased bit density and high sensitivity of mgnetoresistive read heads. There are various types of magneto resistive effects namely, anisotropic magneto resistive effect (AMR), giant magneto resistive effect (GMR) and planar Hall Effect (PHE).

It is a common knowledge that both anisotropic magnetoresistance (AMR) and planar Hall Effect (PHE) are two galvanomagnetic phenomena with the same physical origin [7]. Geometrically speaking, AMR is observed along the current direction, whereas PHE is observed perpendicular to the current. The study of magnetization reversal process in magnetic multilayer using magnetoresistance measurements is rather cumbersome since AMR effect is added on to the GMR effect. The GMR effect depends on the relative orientation of magnetization between neighboring layers, therefore information on the direction of magnetization of each layers is not directly obtained.

PHE effect on the other hand is a powerful tool for analysing the magnetization reversal process in magnetic multilayers because it is sensitive to direction of magnetization in each magnetic layer. The resolution of the angle of the direction of magnetization with respect to the direction of the sense current of PHE is twice better than that of MR, because PHE output voltage oscillates with twice the frequency of GMR [8]. Recently, people have developed a magnetoresistive sensor based on planar Hall Effect for applications to microcompass with angular resolution below $0.5^{\circ}$ [9].

## 1.2 Objectives

The objectives of this project are as follows:

(1) To fabricate magnetic multilayer based planar hall devices using conventional shadow mask technique and lithography process

(2) To investigate the exchange interlayer coupling in magnetic multilayer using a combination of planar hall effects (PHE) and anisotropic magnetoresistance (AMR) measurements

(3) To study the finite size effects of PHE and AMR outputs of magnetic multilayer devices

(4) To compare the AMR and PHE output voltages as a function of the orientation of the constant applied field relative to the current direction

## 1.3 Organization of Thesis

The outline of the thesis is as follows. In chapter 1, the background and the objectives of thesis will be stated. The summary of theories for various MR effect and Planar Hall Effect will be discussed in the Chapter 2. Chapter 2 also reviews the findings of other work relevant to this project. Chapter 3 focuses the device fabrication process such as shadow mask technique, micro fabrication techniques such as photolithography, evaporation, sputtering and lift-off. Experimental results in the interlayer exchange coupling in Co/Cu multilayer is presented in Chapter 4. The role of finite size effects on the exchange coupling is described in Chapter 5. The conclusion and the suggestion of future works based on the results are presented in Chapter 6.

**References**

[1] P. Grunberg, R. Schreiber, Y.Pang, M.B. Brodsky, and H. Sowers, *Phys. Rev. Lett*. 57, 2442 (1986).

[2] S.S.P. Parkin, N. More, and K.P. Roche, *Phys. Rev. Lett*., 64, 2304 (1990).

[3] J.J. Krebs, P. Lubitz, A. Chaiken, and G.A. Prinz, *Phys. Rev. Lett*.,63, 1645 (1989).

[4] J.Unguris,R.J. Celotta and D.T. Pierce, *Phys. Rev. Lett.*, 67, 140 (1991).

[5] G.A Prinz, *Phys. Today*, 58 (1995).

[6] D. J. Mapps, *Sensors and Actuators*, A59, (1997)

[7] D.A Thompson, L.T Romankiw, and A. F. Mayadas, *IEEE Trans. Magn. MAG-11*, 1039 (1975).

[8] T.W. Ko, B.K. Park, J.H. Lee, K.Rhie, M.Y. Kim, J.R. Rhee, *J. Magn. Magn. Mater.* 198-199, 64 (1999).

[9] Francois Montaigne, Alain Schuhl, Frederic Nguyen Van Dau, and Armando Encinas, *Sensors and Actuators*, 81, (2000)

# Chapter 2

# Theory

In order to develop ultra sensitive sensor for data storage applications, it is important to understand the mechanism underpinning the various magnetoresistive effects. In this description, the anisotropic magnetoresistance (AMR), giant magnetoresistance (GMR) and the Planar Hall Effect (PHE) are introduced. The role of interlayer exchange coupling and advantages of planar Hall Effect (PHE) over anisotropic magnetoresistance (AMR) are also discussed in this chapter. A review of related work is also presented.

## 2.1 Magnetoresistance Effect (MR)

Magnetoresistance is the change in electrical resistance of a material due to the presence of a magnetic field [1]. Generally the resistance increases when a field is applied but is non - linear. At high temperatures the change in resistance resulting from the magnetic field is small but at very low temperatures the increase is considerable.

There are different types of magnetoresistance effects, which will be discussed in this chapter.

## 2.2 Anisotropic Magnetoresistance (AMR) Effect

The phenomenon of 'anisotropic magnetoresistance' (AMR) describes the variation of resistivity of ferromagnetic metals as the angle between the current and the magnetization is varied [2]. It is now understood that the AMR in ferromagnetic metals is due to the anisotropic scattering of conduction electrons caused by spin-orbit interaction [3]. Anisotropic magnetoresistance (AMR) has its origins in spin orbit coupling and depends on the relative orientation of magnetization and current directions [4].

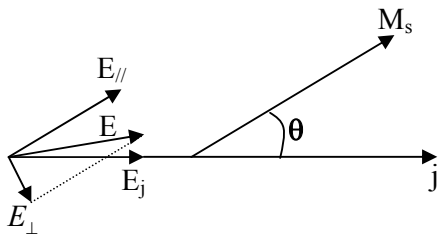


*Fig (2.1) Electrical resistance anisotropy between the parallel and normal directions of magnetization*

The anisotropic magnetoresistance effect is shown in Fig. 2.1. According to Ohm's law, the electrical fields parallel and perpendicular to the magnetization are as follows:

$$E_{//} = \rho_{//} j_{//}, \qquad E_{\perp} = \rho_{\perp} j_{\perp}, \quad \text{----------(2.1)}$$

where

$$j_{//} = j\cos\theta, j_{\perp} = j\sin\theta.$$

The electrical field $\vec{E}$ is not parallel to the current density $\vec{j}$. Its component along the current direction is given by:

$$E_j = E_{//}\cos\theta + E_{\perp}\sin\theta = \rho_{//} j\cos^2\theta + \rho_{\perp} j\sin^2\theta \ . \quad \text{------ (2.2)}$$

The resistivity along the current direction is

$$\rho_j \equiv \frac{E_j}{j} = \rho_{//}\cos^2\theta + \rho_{\perp}\sin^2\theta$$

$$= (\rho_{//} - \rho_{\perp})\cos^2\theta + \rho_{\perp}$$

$$= \rho_0 + \Delta\rho_{\max}\cos^2\theta \qquad \text{---------- (2.3)}$$

where $\rho_0 \equiv \rho_{\perp}, \Delta\rho_{\max} \equiv \rho_{//} - \rho_{\perp}$.

The value of $\frac{\Delta\rho_{\max}}{\rho_0}$ is often called the magnetoresistance (MR) ratio [4]. In here θ is the angle between the magnetization and current direction. In general, the resistivity of an anisotropic MR material will vary according to a cosine square function if the magnetization of the device is rotated with respect to the current direction.

AMR voltage measures between the two adjacent terminals on the film as shown in Fig 2.2 (a).

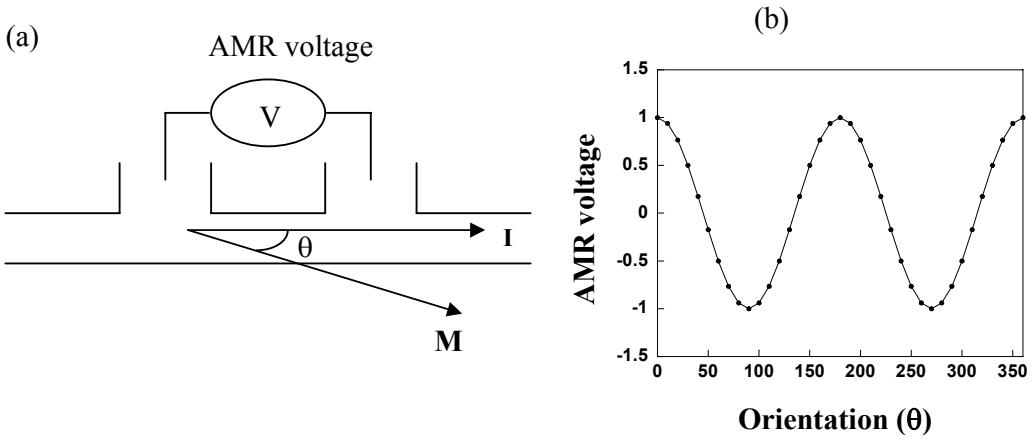


*Fig 2.2(a) Schematic diagram of AMR configuration (b) Typical Graph for AMR vs angle θ*

Shown in Fig 2.2 (b) is a typical plot of the AMR voltage as a function of the orientation of the applied field.

It is clearly seen from this equation (2.3) that when angle $\theta$ is zero, both the current I and the magnetization M are parallel to each other; resulting in a high resistivity.

Anisotropic magneto resistance (AMR) is used in read heads in computer hard disk as a replacement for inductive sensing.

## 2.3 Giant Magnetoresistance (GMR) Effect

GMR was discovered in 1988 by *Baibich et al* [6]. This discovery was due to developments in high vacuum and deposition technology which made possible by the advances is molecular beam epitaxy (MBE) technique capable of depositing thin layers only a few atoms thick. Since the resistance change with magnetic field of up to 70% was observed with GMR as compared to the few percent change in resistance observed in AMR materials, thus the name giant magnetoresistive effect. This has generated interest from both physicists and device engineers, as there is both new physics to be investigated and huge technological applications in magnetic recording and sensors.

GMR describes the behavior of materials that have alternating layers of ferromagnetic and nonmagnetic materials deposited on a non – conducting substrate. Giant magnetoresistance effect can be observed only in a thin film superlattice stack of at least three films: two ferromagnetic layers most typically NiFe or Co, separated by a noble spacer layer, usually Cu [7].

The physics of GMR effect is explained as follows with reference to Figure 2.3. In order to minimize the total energy, the majority of the electron spin directions in the ferromagnetic layers are oriented parallel to the magnetization vector M. When the electric field is applied, the spin – oriented conduction electrons accelerate until they encounter a scattering center, which is the origin of electrical resistivity. The average distance the conduction electron travels is called the coherent length and this length determines the thickness of the nonmagnetic layer, i.e., its thickness must be less than the coherent length.

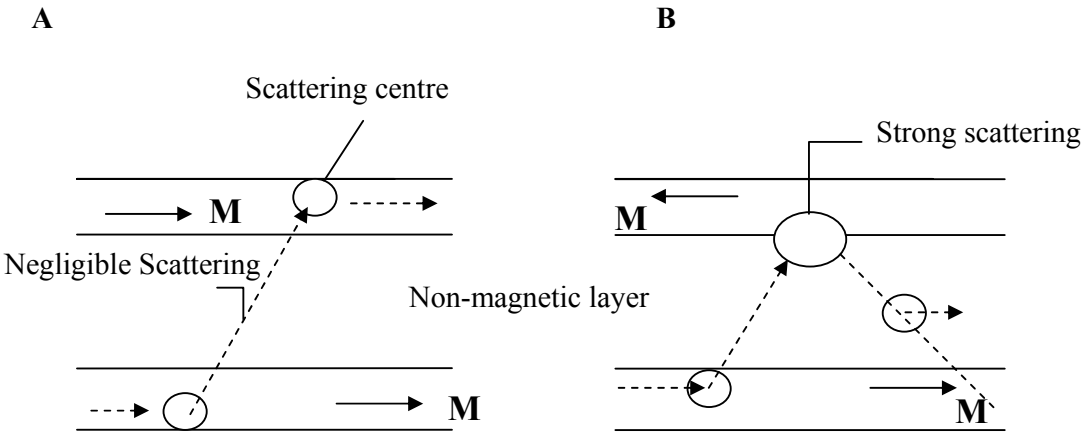


*Fig. (2.3) Schematic diagram of spin state in GMR structure*

When the adjacent magnetic layers are magnetized in a parallel direction, the arriving conduction electron has a high probability of entering the adjacent layer with negligible scattering since the former's spin orientation matches that of the latter layer's majority spins. On the other hand, when the adjacent layer is magnetized in an anti – parallel manner, the majority of the spin – orientated electrons suffer strong scattering at the interfaces because their majority spin orientation do not match. Thus,

when the magnetic layers are in the ferro state (magnetized parallel), the resistance is low and vice versa in the antiferro state (magnetized anti – parallel). GMR is dependent on the relative magnetization directions of the ferromagnetic layers and not on the measuring current direction. This is in contrast to the AMR effect where magnetization – current field angel direction is the important factor.

In short, there are three necessary conditions for the development of GMR. First, the two materials (magnetic and non – magnetic materials) used must be immiscible. Second, the ferromagnetic layers must have some mechanism, be it exchange coupling or mere magnetostatics that establishes the anti – parallel magnetization state in zero external field. Third, the spacer layer material must be thinner than the conduction electron coherence length.

There are many combinations of the ferromagnetic/ nonferromagnetic layers which have been investigated in GMR effect. But only the several most important materials are now in use – Co, Fe, NiFe or NiFeCo alloys separated by Cr, Cu, Ag or Au [8].

The GMR effect is great interest because of its current application of MR read heads in information storage industry.

## 2.4 Planar Hall Effect (PHE)

In addition to the AMR and GMR effects, another galvanomagnetic phenomenon, less popular known and less utilized has been observed in magnetic thin films. This galvanomangetic phenomenon was referred to by Jan [9] as a pseudo Hall effect which was sometimes "improperly" called the "Planar Hall effect". The expression "pseudo-, or planar hall effect" (PHE) has gained acceptance to describe an experiment which has the following characteristics: (1) the output voltage measures an electric field that is perpendicular to the applied current; and (2) the magnetic field vector lies in the plane of the current and voltage electrodes[10]. Planar Hall Effect (PHE) originates purely from AMR and depends on the angle between the magnetization M and the direction of sense current [5, 10]. The investigation of PHE [10-13] has mainly focused on materials such as Fe, Ni, Co and Cu.

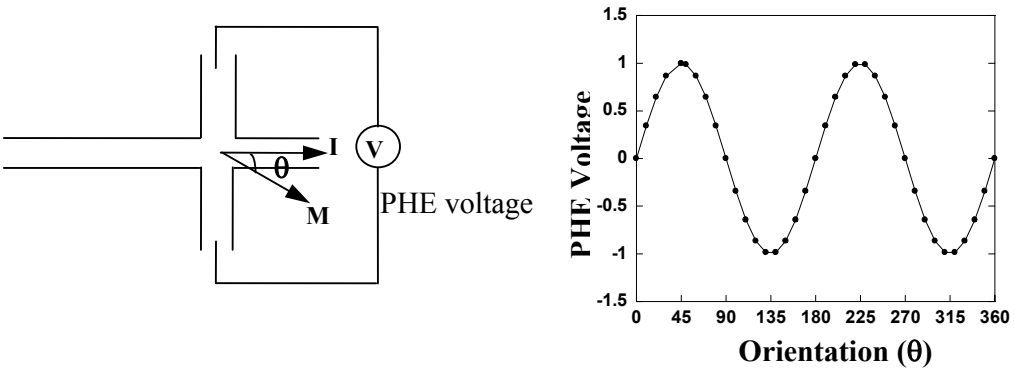


*Fig 2. 4(a) Schematic illustration showing electrical connections for PHE measurement (b) Typical PHE output as a function of field orientation*

Planar Hall Effect occurs when the current I is perpendicular to the voltage probe as shown in Fig. 2.4 (a). The resistivity between the Hall voltage probes reduces to[5]

$$\rho = \rho_0 + \frac{\Delta\rho}{2}\sin(2\theta) \quad \text{---------- (2.4)}$$

where $\Delta\rho = \rho_{//} - \rho_{\perp}$

$\rho_{//}$ = the resistivity when the current is parallel to the magnetization

$\rho_{\perp}$ = the resistivity when the current is perpendicular to the magnetization

$\rho_0$ = the average resistivity of the sample

$\theta$ = the angle between the current and magnetization direction

It can be seen from Eqn (2.4) that while AMR follows $\cos^2\theta$ dependence, the PHE output voltage for a large constant saturation field follows sin 2θ dependence. At low field however when there are domain wall activities, there may be departure from this behavior.

Since PHE is a relatively new development in the field of MR effects, there has yet to be a lot of research work done in this area. Nevertheless, research that has been done on PHE revealed that this effect is capable of determining magnetization directions of individual magnetic layers in multilayer structures as well as to separate magnetization reversal of each neighboring layers. Devices fabricated based on PHE were also shown to give high sensitivity at low detectable field [14].

PHE effect is a powerful tool for analyzing the magnetization reversal process in magnetic multilayer because it is very sensitive to direction of magnetization in each magnetic layer. Moreover, this effect is rather suitable to analyze the magnetization of multilayer for the following reasons. First, the giant magnetoresistance of multilayer

is caused by surface scattering of polarized electrons, while the PHE, in principle, does not depend on surface scattering and, therefore, only the tensorial notation of AMR is to be measured, and the magnetization information could be achieved directly without any effect of GMR [15]. Second, the GMR measurement depends on the relative direction of magnetization between neighboring layers; therefore, the information of the direction of magnetization of each magnetic layer is not directly achieved. One may find the direction of magnetization of each magnetic layer by PHE.

## 2.5 Interlayer Exchange Coupling

The exchange coupling of magnetic films across metallic interlayer was first observed for Dy and Gd films separated by Cr interlayer [16]. After the discovery of interlayer coupling, this coupling has been shown to have an important influence on the magnetic and electric properties of these layered systems, e.g., antiferromagnetic coupling between adjacent ferromagnetic layers can induce a giant magnetoresistance (GMR) [17-19].

The interlayer exchange coupling is the coupling between the magnetic layers that oscillates in sign as a function of the spacer layer thickness. In magnetic multilayers, reflection from the interfaces produces quantum well states, which are spin polarized because the reflection amplitudes are spin dependent. The quantum well states move in energy as the thickness of the spacer layer increases. When they cross the Fermi level, the energy gained or lost from filling them changes the relative energies of the configurations with parallel and antiparallel magnetizations.

The exchange coupling between two layers is usually described by

$$E_{AB} = - J_{AB} \frac{M^A M^B}{M_s^A M_s^B} = -J_{AB} \cos\theta \quad \text{----------} \quad (2.6)$$

where $J_{AB}$ (erg $cm^{-2}$) is the interlayer exchange coupling

$M^A$ and $M^B$ represents the total magnetic moments for layers A and B

$M_s$ is saturation magnetization

and $\theta$ is the angle between the magnetic moments [20].

The magnitude of the GMR effect oscillated as the thickness of the nonferromagnetic space between the ferromagnetic layers was increased. This oscillation was shown to be caused by an oscillation in the sign of the interlayer exchange coupling between the ferromagnetic materials. The coupling was shown to oscillate between the antiferromagnetic and ferromagnetic coupling such that the magnetic moments of successive ferromagnetic layers were either parallel (ferromagnetic) or antiparallel (antiferromagnetic) in small fields.

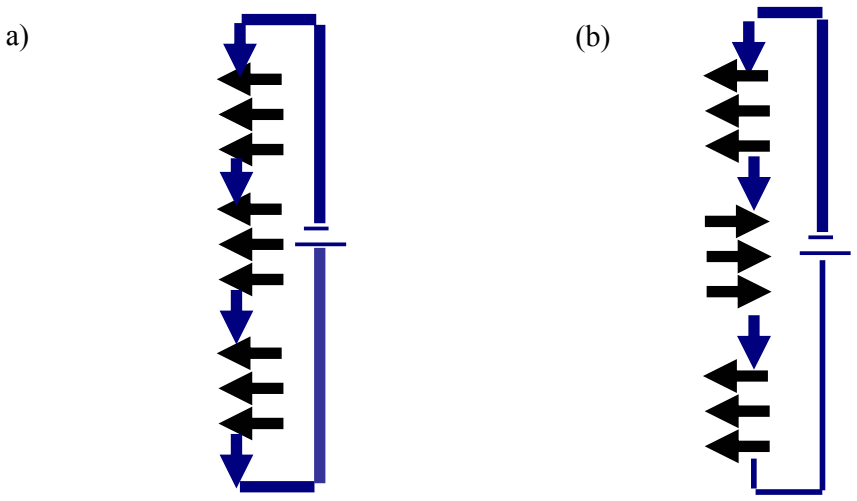


*Fig 2.5 FM layers with magnetic order correlated by the (a) FM and (b) AFM exchange coupling*

In this project, we have investigated the exchange mechanism in Co/Cu and NiFe/Cu multilayer structures as follows.

In recent years especially Co/ Cu system has drawn attraction. One reason for this is that Co / Cu is a suitable candidate for verifying theoretical predictions on the period (s) of oscillations in the exchange coupling strength as a function of Cu spacer layer

thickness. Another reason is that ferromagnetic cobalt layers separated by thin copper layers, was found to exhibit very large GMR effects even at room temperature [21, 22]. Values of GMR in Co/Cu multilayers exceed 110% at room temperature [22].

The Co/ Cu multilayer structure is used for potential applications in sensors. These multilayers also provide attractive sensitivity, coupled with good thermal stability.

**References:**

[1] John C. Mallinson, Isaak D. Mayergoyz, "*Magnetoresistive Heads: Fundamental and Applications*", Hard covered, 1995

[2] W. Thomson., *Proc. R. Soc. London* 8, 546 (1857)

[3] B. Dieny, M. Li, S.H. Liao, C. Horng, and K. Ju, *J. Appl. Phys*., 88, pp 4140-4143

[4] Shan X. Wang and Alexander M. Taratorin, "*Magnetic Information Storage Technology*", Academic Press, 1999.

[5] F. Nguyen Van Dau, A. Schuhl, J. R. Childress and M. Sussiau, *Sensors and Actuators* A 53 (1996)

[6] M.N Baibich,., J. M. Broto, A Fert, F. Nguyen Van Dau, F. Petroff, P. Eitenne, G. Creuzet, A. Friederich and J. Chazelas, *Phys. Rev. Lett*., 61 (1998)

[7] http://crism.stanford.edu/~web/webpage/gmr.pdf

[8] S. Tumanski., "*Thin Film Magnetoresistive Sensors*", Institute of Physics Publishing, 2001

[9] J. P. Jan, "Advances in research and application", *Solid State Physics*, vol 5, 15 (1957)

[10] D.A. Thomson, L.T.Romankiw, A.F. Mayadas, *IEEE Trans. Magn*. MAG-11 1039 (1975).

[11] L. Berger, *J. Appl. Phys*. 69(3) (1991) 1550

[12] J.H.Fluitman, *J.Appl. Phys*. 52(3) (1981) 2468

[13] B. Zhao, X.Yan, A.B. Pakhomov, *J.Appl. Phys*. 81 (8) (1997) 5527

[14] T.W. Ko, B.K. Park, J.H. Lee, K.Rhie, M.Y. Kim, J.R. Rhee, *J. Magn. Magn.Mater.* 198-199, 64 (1999).

[15] J.H. Lee, B.K. Park, K. Rhie, G. Choe, K. H. Shin, *J.Magn. Magn. Mater*. (198-199) 1999

[16] P. Bruno, *J. Magn. Magn. Mater*. 121, 248 (1993); *Phy. Rev. B.* 52, 411 (1995)

[17] M. N. Baibich, J. M. Broto, A. Fert, F. Nguyen Van Dau, F. Petroff, P. Eitenne, Creuzet, A. Friedrich, and J. Chazelas, *Phys. Rev. Lett*. 61 (1988)

[18] S.S.P. Parkin, N. More, and K.P. Roche, *Phys. Rev. Lett*., 64, 2304 (1990).

[19] F.Petroff, A. Barthelemy, D.H. Mosca, O.K. Lottis, A. Fert, P.A. Schroeder, W. P. Pratt Jr. and R. Loloee, *Phys. Rev.* B44 (1991)

[20] B. Heinrich and J. F. Cochran, *Advanced in Physics*, 1993

B.C. Lee, Y.-C. Chang, *Phy. Rev.* ***B***, 62 (2000)

[21] S. S. P. Parkin, R. Bhadra, and K. P. Roche, *Phys. Rev. Lett.* **66,** 2152 (1991).

[22] S. S. P. Parkin, Z. G. Li, and D. J. Smith, *Appl. Phys. Lett.* **58,** 2710 (1991).

# Chapter 3

# Experimental Techniques

In Chapter 2, we have introduced the theoretical description of the MR and PHE effects. Here, we will introduce the experimental techniques involved in the fabrication of MR and PHE devices. The steps and flow chart for the device fabrication is discussed in this chapter. This fabrication includes wafer cleaning, lithography, developing process, evaporation, lift off, sputtering and wire bonding process.

## 3.1 Fabrication of Planar Hall Devices by Using Shadow Mask

### 3.1.1 Layout of Masks

In the fabrication process using conventional shadow mask technique, two different masks were used. The first one is used for deposition of active region and the second one is used for the deposition of contact pads to the devices.

The mask layout sketches used are shown below.

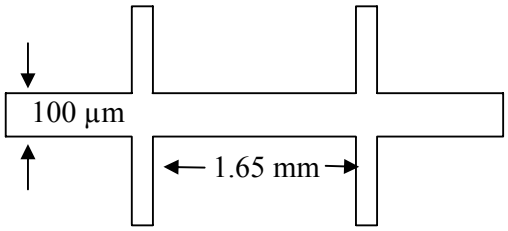


*Fig. 3.1 Mask used for deposition of materials for planar hall device*

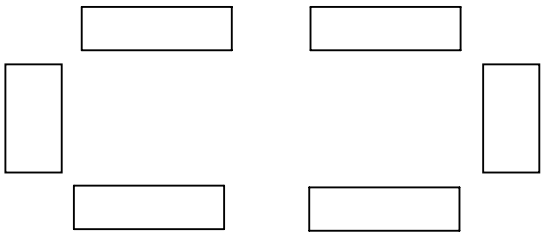

*Fig 3.2. Mask used for deposition of contact pads for device*

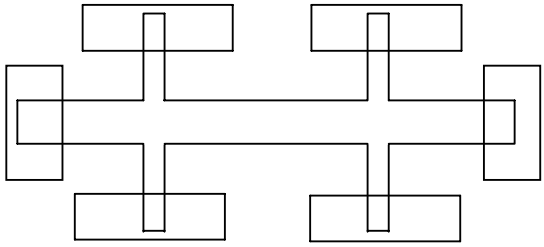

*Fig 3.3 Schematic diagram of the device after aligning*

### 3.1.2 Steps for shadow mask technique

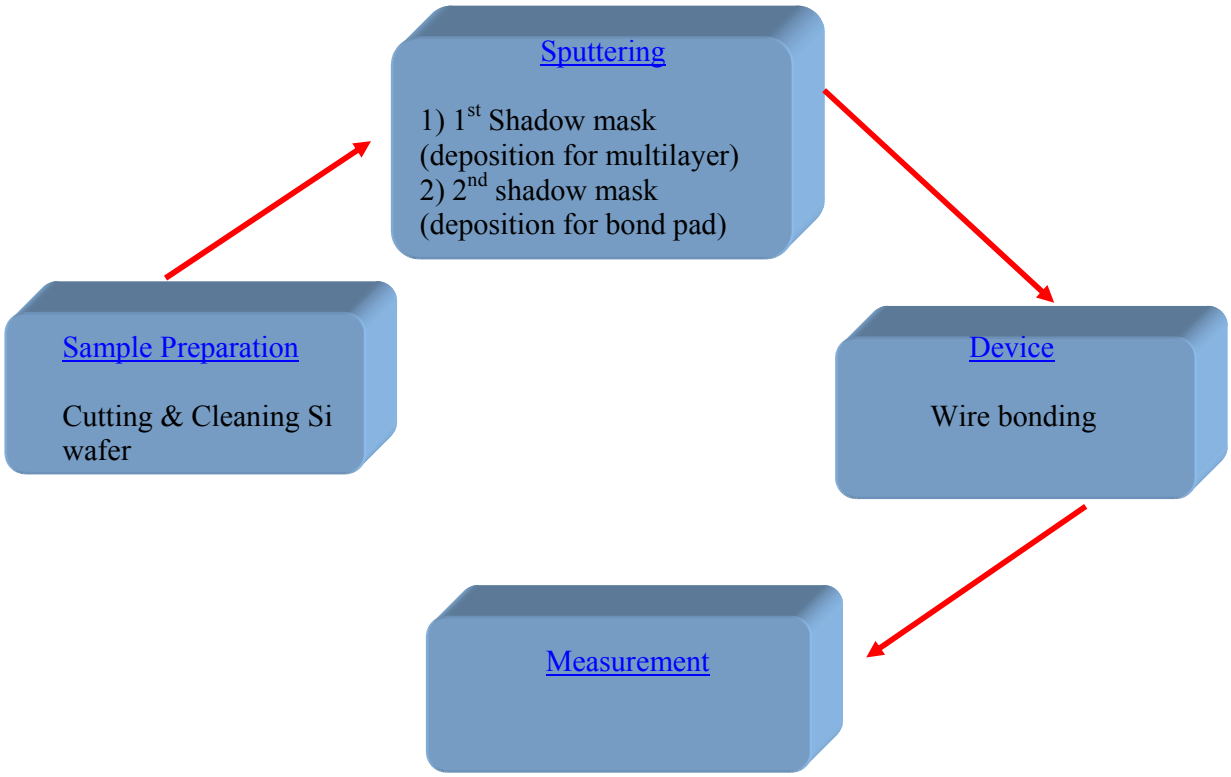


*Fig. 3.4 Steps for fabrication of devices by shadow mask technique*

### 3.1.3 Cleaning of silicon wafers

In any fabrication process, wafers have to undergo intensive cleaning process before they are being fabricated into devices. In this cleaning process, the diced wafers of 1.1 cm x 1.1 cm were soaked in acetone beaker and this beaker was kept in the ultrasonic system for more than 30 minutes. After ultrasonic agitation, these diced wafers were transferred into the isopropanal beaker and finally rinsed in DI water. After rinsing, the cleaned wafers are baked for more than 10 minutes at 90 °C. The next stage in the fabrication process is the deposition of magnetic multilayer using sputtering technique.

### 3.1.4 Sputtering

In our conventional shadow mask technique, the important and unique deposition method is sputtering. The main idea of the sputtering method is presented in Fig. 3.4.

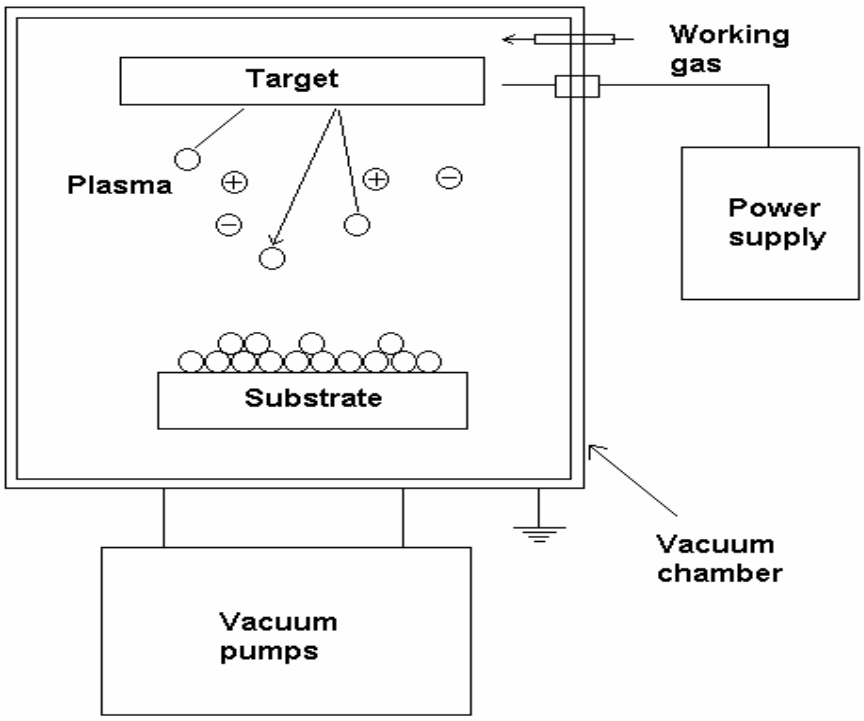


*Fig. 3.5 Schematic diagram of the sputtering process*

Vacuum deposition of magnetic thin film through sputtering is the preferred method used in thin film and hard disk technology. Sputtering is accomplished by applying a voltage between the target material and the substrate to be sputtered in a vacuum vessel containing a sputtering gas Argon (Ar). Argon is universally used due to its low cost and larger atomic mass, leading to good sputtering yields.

Plasma of electrons and Ar ions is spontaneously generated upon voltage application and the Ar gas glows purple from the electronic excitations. Argon ions are accelerated onto the target material, and by momentum transfer; atoms are displaced from the target and transferred to the substrate.

*Fig. 3.6 Cryo Vac thin film Deposition System*

Fig. 3.5 shows the sputter machine system used in this project. This system is called "Cryo Vac Thin Film Deposition System". There are two main chambers in this system, main chamber and load lock chamber. The cleaned 1.1 cm x 1.1 cm Si wafers were loaded on the substrate holder in the load lock and then transferred to the main chamber using a transferring rod. After reaching the good pressure (4.7 x $10^{-7}$ Torr), the samples were deposited using Co and Cu target materials.

### 3.1.5 Fabrication Procedure for Shadow Mask Technique

Firstly, Co/Cu multilayers were deposited by DC sputtering at 10mTorr Ar gas pressure onto a six terminal device shadow mask (shown in Fig. 3.1) placed on top of a Si (100) substrate at a deposition rate of 1.1 Å /s for Co. The deposition rate for Cu is 2.1 Å /s. In all the samples, 4 Co/Cu bilayer were deposited. The devices were capped with a 4 nm of Cu film to prevent the devices from oxidation. In the second stage of the fabrication, electrical contacts were made by aligning another shadow mask (shown in Fig. 3.2) to the six terminal devices in the first process step, followed by the deposition of 3000 Å (300nm) of Aluminium at rate of 1.2 Å/s using DC sputtering. The details of sputtering parameters are listed in Table 3.1 and Table 3.2.

| | |
|---|---|
| Sputtering Type | DC sputtering |
| Sputtering Materials | Co, Cu |
| Base pressure | $4.6 \times 10^{-7}$ Torr |
| Sputter Power | 100 W |
| Ar gas Flow Rate | 10 sccm |
| Ar gas pressure | 10 mTorr |
| Deposition rate for Co | 1.1 Å/s |
| Deposition rate for Cu | 2.2 Å/s |

*Table 3.1 Sputter parameters for Co/Cu multilayer structure*

| | |
|---|---|
| Base Pressure | 4.7 x10 -7 Torr |
| Sputtering Type | DC |
| Sputtering Gas | Argon (Ar) |
| Gas Flow Rate | 10 sccm |
| Gas Pressure | 10 mTorr |
| Film Deposition Rate | 1.2 Å/s |
| Film Thickness | 3000 Å (300 nm) |
| Sputtering Power | 200 W |

*Table 3.2 Sputter parameters for Al bond pads*

In order to dice the devices to 5 $mm^2$ series, the samples were coated with optical resist to prevent the devices from being damaged during dicing. Shown in Fig 3.6 is the spin coater used.

*Fig. 3.7 Photo of the spin coater*

### 3.1.6 Wire Bonding

Wire bonding today is used throughout the microelectronics industry as a means of interconnecting the chips, substrates and output pins. There are three fundamental wire bond methods which have been developed over the years in the semiconductor history. These methods are identified as thermocompression (T/C), ultrasonic (U/S) and thermosonic (T/S) bonding [1, 2]. Most commonly used materials are gold and aluminum. Available bonding techniques are identified as "ball" and "wedge" bonding [1, 2, 3].

In the wire bonding process in this project, the samples were mounted into the 24- pin chip packages using silver paint. Now, the chip packages are ready for bonding using gold wire. The choice of material of the wire depends on the requirement of the user application. In this project, Model 4523AD Wedge Wire Bonder (thermosonic) was used. The photo of wire bonder is shown in Fig.3.7.

*Fig. 3.8 Photo of Wire Bonder (4523AD)*

The parameters used are shown in Table 3.3.

| To substrate | To chip carrier |
|---|---|
| Force = 1.4 (40 gm) | Force = 2.2 (60 gm) |
| Power = 1.76 W | Power = 1.98 W |
| Time = 6.0 s | Time = 9.9 s |

*Table 3.3 Wire bonding parameters*

## 3.2 Fabrication of Planar Hall Devices by Using Photolithography Process

### 3.2.1 Masks

In lithography process for the device fabrication, two optical litho masks were used. The first mask used for the patterns for planar hall bar is shown in Fig. 3.9.

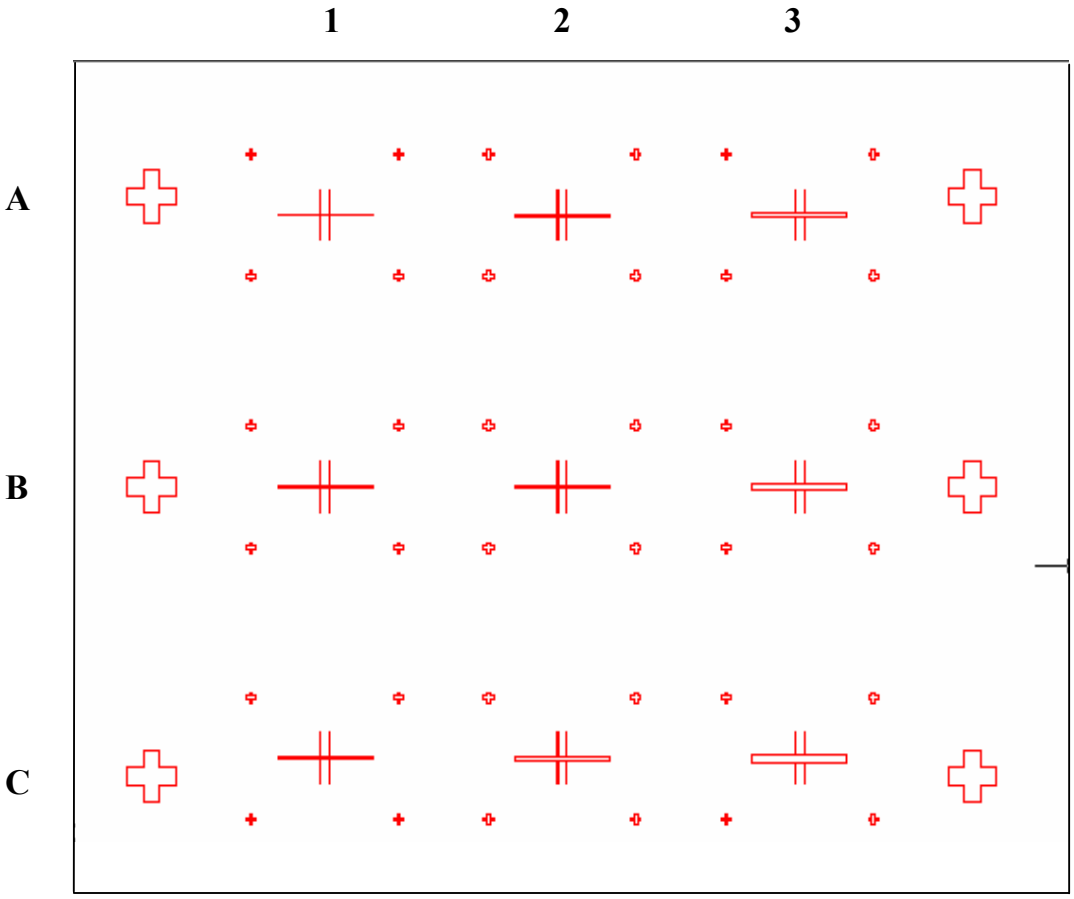


*Fig. 3.9 Mask for the first layer of planar hall devices*

There are nine devices on the mask and these structures are identical except that they have different "width" dimensions.

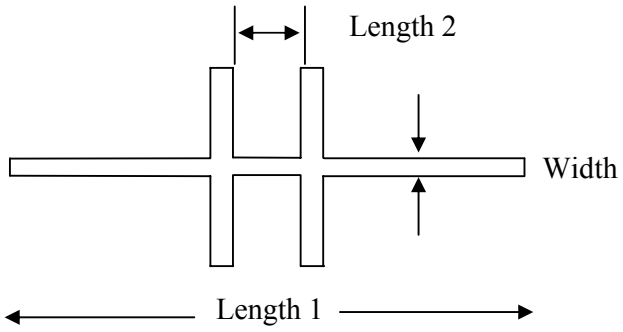


*Fig. 3.10 Basic sketch for the device*

A summary of dimensions is given in Table 3.4.

| Devices | A1 | B1 | C1 | A2 | B2 | C2 | A3 | B3 | C3 |
|---|---|---|---|---|---|---|---|---|---|
| Length 1 (μm) | 50 | 50 | 50 | 50 | 50 | 50 | 50 | 50 | 50 |
| Length 2 (μm) | 5 | 5 | 5 | 5 | 5 | 5 | 5 | 5 | 5 |
| Width (μm) | 3.5 | 5 | 7 | 10 | 15 | 20 | 30 | 40 | 50 |

*Table 3.4 Dimensions for the planar hall device mask*

The second mask consists of nine contact pad patterns as shown in Fig. 3.11.

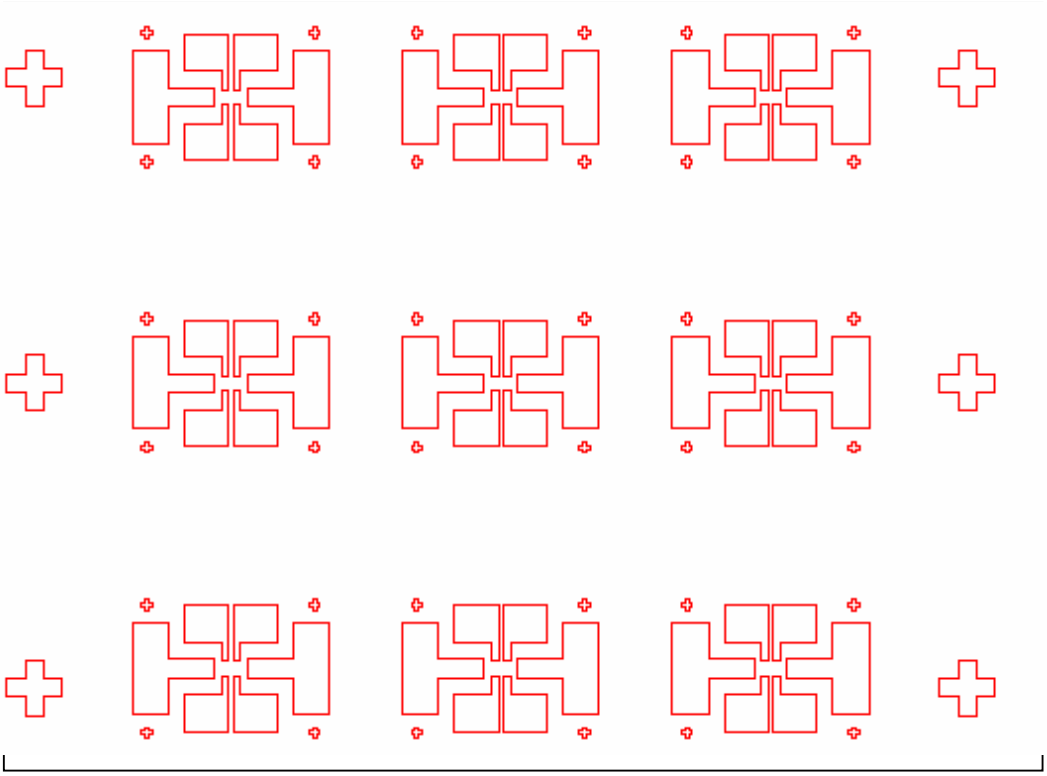

*Fig. 3.11 Mask for the second layer of contact pads*

The first mask was used to form the first layer of patterns on the Si wafer followed by the second mask which lays the contact pads on the devices for measurement purposes.

### 3.2.2 Photolithography Process

Lithography is the process used to transfer the patterns from the mask to the Si substrate. The most common one uses ultraviolet and is called photolithography. There are two parts in the lithography mask, the “clear” and the “chrome” part, which is opaque. Fig. 3.12 illustrates schematically the lithographic process used to fabricate

the devices. The exposing radiation is transmitted through the "clear" parts of a mask. The pattern of opaque chromium blocks some of the radiation.

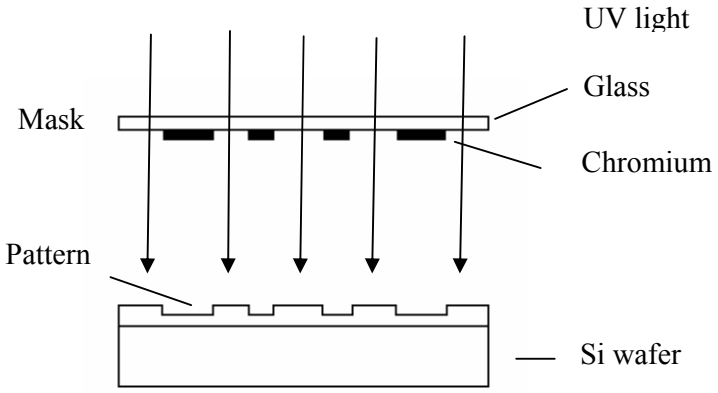


*Fig. 3.12 Schematic diagram of photolithography process*

Before doing lithography process, the diced 5.5 mm x 5.5 mm samples were be cleaned using ultrasonic. In cleaning process, the diced wafers of 5.5 mm x 5.5 mm were soaked in acetone beaker and this beaker was kept in the ultrasonic system for more than 30 minutes. After ultrasonic agitation, these diced wafers were transferred into the isopropanal beaker and finally rinsed in DI water. After rinsing, the cleaned wafers are baked for more than 10 minutes at 90 °C.

The cleaned substrates are coated with a layer of photoresist. There are two identifications of resists, positive and negative resists. Both resists are a mixture of a photoactive material, a resin and a solvent. Positive resist is initially insoluble in the developing solution but it becomes soluble after exposure to UV light. Negative resist, however, is initially soluble in the developer and it becomes insoluble after exposure to UV light. Comparing the 2 types of resists, positive resist has poorer adhesion and is less sensitive (require longer exposure time), but it has higher resolution than negative resist.

The photoresist used in this fabrication process was positive photoresist AZ 7220. The properties of AZ 7220 series are as follows:

- high speed with high contrast and high resolution.
- good dry etching stability.
- excellent pattern profile in thick film processes.
- wide exposure latitude.

The specifications of AZ 7200 are shown in Table (3.5).

| | |
|---|---|
| Viscosity ( $25°C$ ) | $9.7 \pm 1.0$ |
| Specific gravity | $1.035 \pm 0.010$ |
| Water content (wt%) | 0.5 max |
| Principal Solvent | - propylene glycol monomethyl ether acetate |

*Table 3.5 The chemical and physical properties of AZ 7220 photoresist series [4]*

The photo resist was dropped on the cleaned Si wafer and spun at 4000 rpm for 30sec. The resist-coated samples were then baked for 30 minutes in an oven at 90 C (soft baking). The patterns were made from the mask by exposing through the ultra-violet (UV) light using the system MA6. Fig. 3.13 shows the Karl-Suss Mask Aligner system (MA6) used.

*Fig. 3.13 Photo of Mask Aligner (MA6)*

After exposure, the samples were then developed in the AZ developer 300 MIF mixed with DI water in the ratio 4:1 for about 45 s, rinsed in DI water, and blown dry with $N_2$ gas. The samples were checked under the microscope to make sure the patterns were properly developed before they are ready for evaporation.

The flowchart of the fabrication process is shown in Fig 3.14.

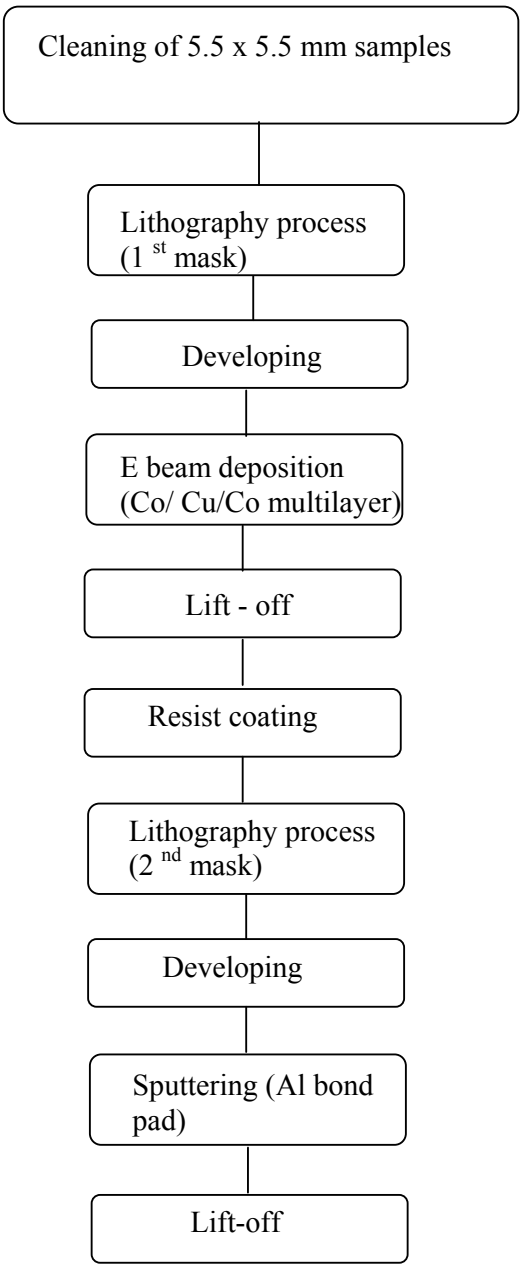


*Fig. 3.14 Steps for device fabrication using lithography process*

The actual process step is shown in Fig. 3.15.

Step 1 Cleaned Si wafer

Cleaned Si wafers

Step 2 Photoresist on Si wafer

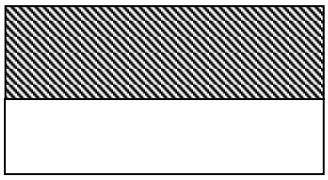

Photoresist

Si wafers

The positive photoresist was spun on the Si wafers at 4000 RPM for 30 sec. The coated Si wafers were then baked at 90° C for 30 min.

Step 3 First Exposure

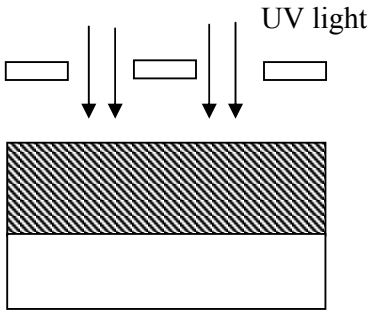


1st Mask

Photoresist

Si wafers

Exposed for 11 sec.

Step 4 After development

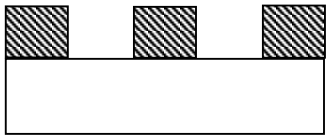

Photoresist

Si wafers

The exposed wafer was developed in AZ 300 MIF (4:1) solution for 45 sec.

Step 5 Multilayer deposition

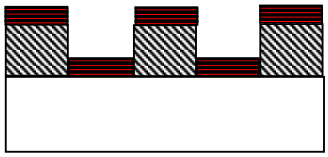

Co/Cu or NiFe/Cu ML

Photoresist

Si wafers

The Co/Cu or NiFe/Cu multilayers were deposited using e beam deposition onto the Si patterned samples.

Step 6 After Lift Off

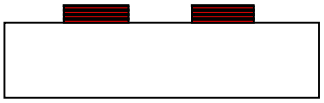

Co/Cu or NiFe/Cu ML
Si wafers

The Co/Cu or NiFe/Cu multilayers were deposited onto the Si patterned samples.

Step 7 Coating the 2nd layer of photoresist layer

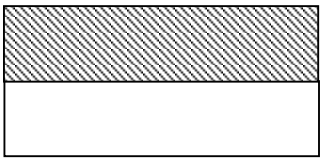

Photo resist
Co/Cu or NiFe/Cu ML
Si wafers

The positive photoresist was spun on the patterned Si wafers at 4000 RPM for 30 sec. The coated Si wafers were then baked at 90° C for 30 min.

Step 8 2nd exposure

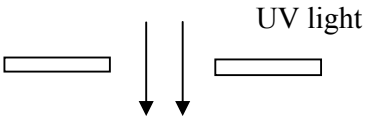


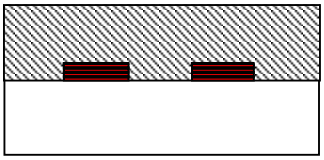

Photo resist
Co/Cu or NiFe/Cu ML
Si wafers

Exposed for 11 sec.

Step 9 After 2nd developing

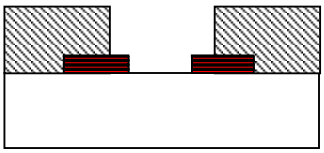

Photo resist
Co/Cu or NiFe/Cu ML
Si wafers

The exposure samples were developed in AZ 300MIF (4:1) developer solution for 40 sec.

Step 10 After deposition

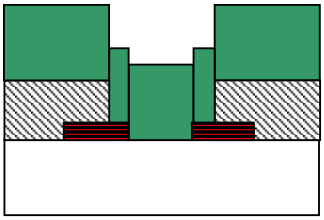


Step 11 After Lift off

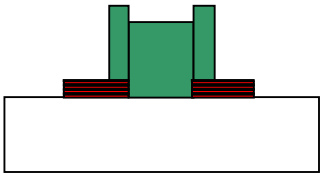


*Fig. 3.15 Fabrication steps using photolithography process*

### 3. 2. 3 Evaporation

Another technique used in the deposition of Co/Cu and NiFe/Cu multilayers is electron beam evaporation. In this project, the Korea Vacuum Technology (KV 2000) system is used. The evaporator system is shown in Fig. 3.16. There are two modes in this system, thermal and e-beam evaporation.

Thermal evaporation is one of the most commonly used metal deposition techniques. It consists of vaporizing a solid material (pure metal, eutectic or compound) by heating it to sufficiently high temperatures and reconsidering it onto a cooler substrate to form a thin film [5]. As the name implies, the heating is carried out by passing a

large current through a filament container (usually in the shape of boat). This then causes the container to heat up and allows the material to simply evaporate. The choice of the filament material is dictated by the evaporation temperature and its inertness to alloying/ chemical reaction with the evaporant. Good vacuum is a prerequisite for producing contamination free deposits.


*Fig. 3.16 Picture of Evaporator System (EV 2000)*

The second form of evaporation is the electron beam deposition technique. The system has a tungsten filament, which acts as a source of electron beam. The current is passed through the filament wire, from which electrons are emitted. The beam is focused on the crucible, with the help of applied magnetic field. The direction of the

beam can be changed both laterally and longitudinally. This is done by changing the direction of the magnetic field. Amplitude of the beam can be varied by varying the strength of the magnetic field. Amplitude of the beam signifies the sharpness of the beam. Generally, materials having high melting point are used for electron beam deposition.

The whole evaporation system is a custom built system comprising a turbo pumping system backed by a rotary pump. The base pressure is of the order of $10^{-7}$ mbar. The stage comprises a temperature control system to produce more accurate film growth. . The system is fitted with a sensor crystal used for sensing the thickness of the materials deposited. The thickness sensitivity mechanism is connected to the LG monitor where all the deposition parameters can be controlled.

The materials used for thin film deposition in the project are Co, Cu and NiFe (Permalloy). These materials are used for making multilayer structures on Si (100) substrate. Because there is a lateral distance between the crystal detector used for in-situ monitoring of the deposited films and the substrate, it is necessary to determine the ratio of respective amounts of deposits between these two surfaces. This ratio is known as the "tooling factor" and is a unique quantity for a particular evaporator, which depends on a number of factors including the dimensions of the system and the actual evaporant. Table 3.6 shows these values are given for the materials used in the project.

| **Metal** | **Density (gm/cm3)** | **Zfactor (Acoustic Impedence)** | **Tooling Factor (%)** |
|---|---|---|---|
| Cu | 8.93 | 0. 49 | - |
| Co | 8.71 | 0.44 | 100% |
| NiFe (Permalloy) | 9.1 | 1.0 | 120% |

*Table 3.6 The summary for the materials used in this fabrication and properties*

### 3.2.4 Lift Off

After evaporation or sputtering, the sample were removed from the chamber and immersed in acetone to dissolve the resist. The Si samples were soaked in acetone for a couple of minutes to remove the remaining photo resist together with the materials deposited on it. Then the devices were rinsed in iso-propanol and transferred to the Deionized (DI) water and then finally blown dry by nitrogen. The time for complete lift off varied from minutes to hours according to different dimensions of the patterns and different deposition conditions.

### 3.2.5 Sputtering and Wire Bonding

As shown in shadow mask technique, we used the same procedure and process for sputtering and wire bonding. But in lithography process, after deposition Al for bond pads using sputtering machine, the samples had to do lift off.

After lift off, the samples were successfully bonded in 24-pin chip carrier. Since there were nine devices on one Si wafer and each device has six – terminals, a maximum of

four devices to be bonded onto was based on the ease of bonding. Devices B2, B3, C1 and C2 (see Fig. 3.7 and Table (3.4) were bonded. But some of the devices were not successfully bonded in some samples.

## 3. 3 Characterization Techniques

### 3.3.1 Four Point Probe Method

The magneto transport measurement set up picture for all the measurements is shown in Fig. 3.17.

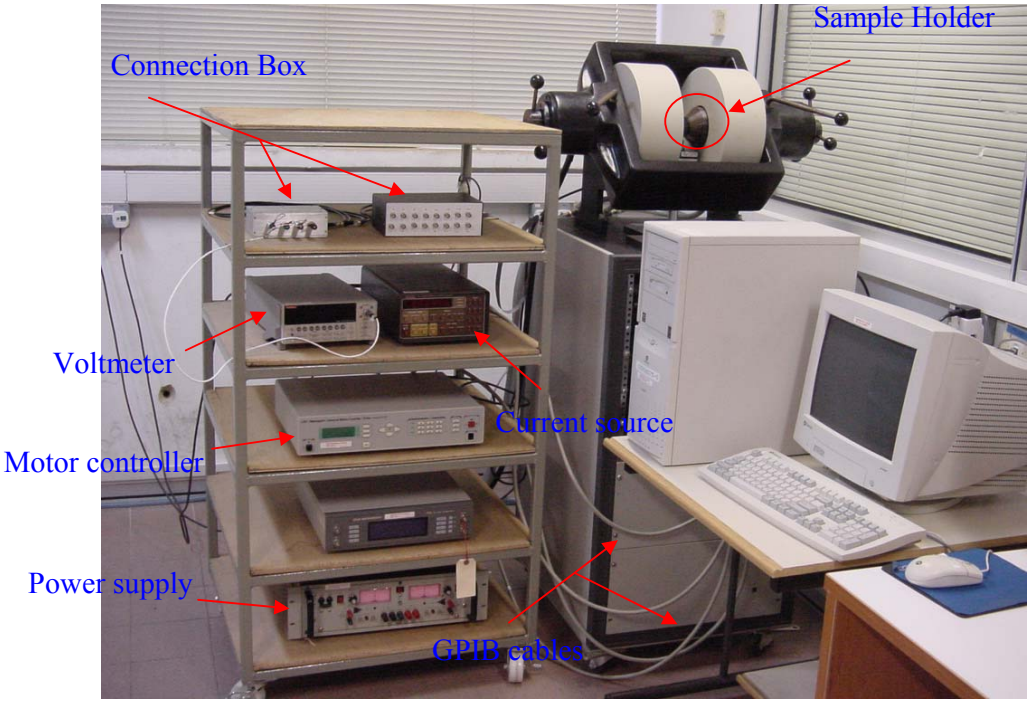


*Fig. 3.17 Magnetotransport measurement set up system*

The completed device is inserted into the chip holder of the magneto transport machine shown by the enclosed circle in Fig. 3.13. This is in turn connected to the connection box that has 24 pin sockets.

A Keithley precision current source was used for the current flowing through the sample. The voltage drop across the sample ($V_{23}$ for AMR and $V_{35}$ for PHE) was measured by 2182 nano voltmeter. The acquisition of data was performed automatically through computer interface.

The magnetic field induced by the electromagnet can be varied accordingly using the remote program that was developed with Lab View 5.1 software in house [6].

### 3.3.2 Vibrating Sample Magnetometer (VSM)

The Vibrating Sample Magnetometer (VSM) measures the magnetic properties of materials. Magnetic properties such as coercivity ($H_c$), saturation magnetization ($M_s$), squareness ratio ($S^*$), remanent magnetization ($M_r$) can be obtained from VSM measurements. The Schematic illustration of VSM is shown in Fig. 3.18.

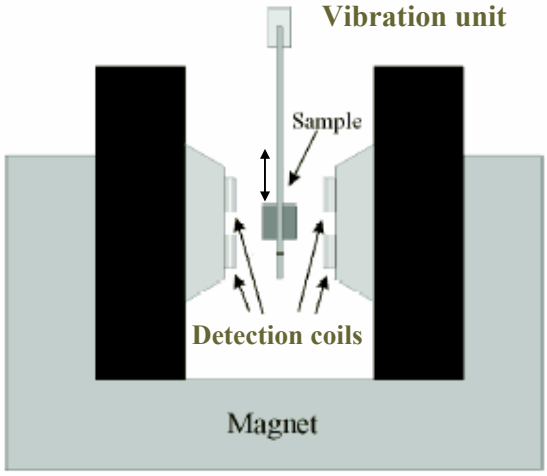


*Fig. 3.18 Schematic Diagram of Vibrating Sample Magnetometer (VSM) [7]*

When a sample is placed within a uniform magnetic field and made to undergo sinusoidal motion (i.e. mechanically vibrated), there is some magnetic flux change. This flux change will induce a voltage in the pick-up coils of the VSM.

According to Faraday's law, the flux change caused by the moving magnetic sample causes an induction voltage across the terminals of the pick – up coils which is proportional to the magnetization of the sample according to the equation (3.1).

$$V_{ind} = -N\frac{d\phi}{dt} \qquad \text{---------- (3.1)}$$

where $V_{ind}$ represents the flux in the pick – up coils caused by the moving magnetic sample, C is constant.

The instrument displays the magnetic moment of the sample in emu units.

**Reference:**

[1] George G. Harmon, "Wire bonding in microelectronics: materials, processes, reliability, and yield**",** McGraw-Hill, c1997

[2] Malcolm R. Haskard, "Electronic circuit cards and surface mount technology: a guide to their design, assembly, and application", New York: Prentice Hall, c1992

[3] Daryl Ann Doane, Paul D. Franzon**, "**Multichip module technologies and alternatives: the basics", New York : Van Nostrand Reinhold , c1993

[4] Clariant Product Catalogue on AZ Resists, Clariant (Japan) K.K

[5] http://www.betelco.com/sb/c34.html

[6] Wang Chen Chen, "Development of a real time data acquisition package for magnetoelectronic devices", 2002.

[7] http://www.el.utwente.nl/tdm/istg/research/vsm/vsm.htm

# Chapter 4

# Interlayer Exchange Coupling in Magnetic Multilayer Films

## 4.1 Overview

In this chapter, the interlayer exchange coupling effects and magnetization reversal of Co/Cu and NiFe/Cu multilayer magnetic films are investigated using magneto transport and vibrating sample magnetometer measurements. The devices were fabricated using shadow mask technique described in section (4.3). We have investigated the role of spacer layer thickness in the magnetization reversal in the multilayer films.

## 4.2 Introduction

In recent years, coupling of ferromagnetic layers in multilayer and sandwich films, through the non-magnetic metallic layers, has generated considerable interest [1-3]. Interest has been focused on the spin valve structures consisting of two ferromagnetic layers separated by a non- magnetic layer because of its application to magnetoresistive sensors and magnetic random- access memories. Many magnetic multilayer systems exhibit a coupling between the magnetic layers mediated by the non-magnetic spacers, which oscillated periodically between ferromagnetically (FM) and antiferromagnetic (AFM) as the spacer layer thickness varies in the range of 0.5-5 nm [3-6]. Interlayer exchange has been shown to have an important influence on the magnetic properties of these layered systems e.g., Co/Cu and NiFe/Cu. For example,

anitiferromagnetic coupling between adjacent ferromagnetic layers can be used induce giant magnetoresistance (GMR) effects. Various experimental methods have been used to study the physical mechanism controlling the interlayer coupling.

P. Grunberg et.al [4] reported that a continuous decrease of exchange coupling to zero as the Au thickness is increased from 0 to ≈ 2 nm for Au interlayer in Fe/Au/Fe film structure. Similarly, S.S.P. Parkin et.al [3] have studied the anitiferromagnetic interlayer exchange coupling and enhanced magnetoresistance in two metallic systems, Co/Cr and Co/Ru. In these systems and in Fe/Cr superlattices both the magnitude of the interlayer magnetic exchange coupling and the saturation magnetoresistance are found to oscillate with the Cr or Ru spacer layer thickness with a period ranging from 1.2 nm in Co/Ru to ≈ 2.1 nm in the Fe/Cr and Co/Cr systems. S. Honda et.al [8] showed that the magnetoresistance increases monotonically with the Cu spacer layer thickness ($t_{Cu}$) up to 4 nm resulting from the decoupling between the ferromagnetic layers in zero biased films.

In the present work, we have investigated the magneto transport and magnetization reversal process in magnetic multilayer made of Co/Cu. We have studied the interlayer exchange coupling by varying the thickness of spacer layer while keeping the thickness of magnetic layers unchanged.

## 4.3 Fabrication Procedure

In shadow mask technique, two different masks are used as shown in Fig 3. Firstly, the Si substrates were thoroughly clean using ultrasonic with acetone and isopropanol (IPA). Co/Cu multilayers were deposited by DC sputtering onto a six terminal device shadow mask placed on top of a Si (100) substrate. The Ar pressure during the sputter process was 10 mTorr, the Co deposition rate was 1.1 Å/s, and the deposition rate for

Cu was 2.2 Å/s. The thickness of the individual magnetic Co layer was in 100 Å (10 nm) each. The thickness of the spacer layer ranges from 0 to 15 nm. In all the samples, 4 Co/Cu bilayer were deposited and then a 3nm-capping layer of Cu was over coated to protect the devices from the oxidation.

A cross section of the layer structure is presented in Fig. 4.1.

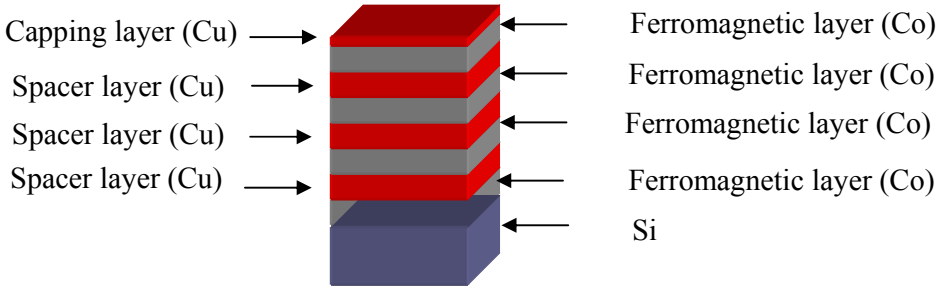


*Fig. 4.1 Layer structure of the Co/Cu/Co multilayer*

In the next stage of the fabrication, electrical contacts were made by aligning another shadow mask to the six terminal device in the first process step, followed by the deposition of 300 nm of Aluminum at the deposition rate of 1.2 Å/s using DC sputtering. In all deposition process, the base pressure of the main chamber was maintained at 4.7 X $10^{-7}$ Torr.

After completing the deposition of materials for the planar hall device and its contact pads, electrical contacts of the hall bar device are made to the six Al bond pads using 24- leadless pin chip carrier using gold wire.

## 4.4 Magnetization reversal in [Co (10 nm)/Cu ($t_{Cu}$) /Co (10 nm)]$_2$ multilayer films

In this section, we present the experiment results of the magnetic properties of magnetic multilayer [Co (10 nm) /Cu ($t_{Cu}$) /Co (10 nm)]$_2$ as a function of Cu spacer layer thickness ($t_{Cu}$) after field applied along the easy axis.

In order to investigate the magnetization reversal process, references samples were loaded in the deposited chamber along the shadow mask samples for all $t_{Cu}$. The reference samples were then characterized using Vibrating Sample Magnetometer (VSM). Shown in Fig. 4.2 are representative M – H loops for various Cu spacer layer thicknesses.

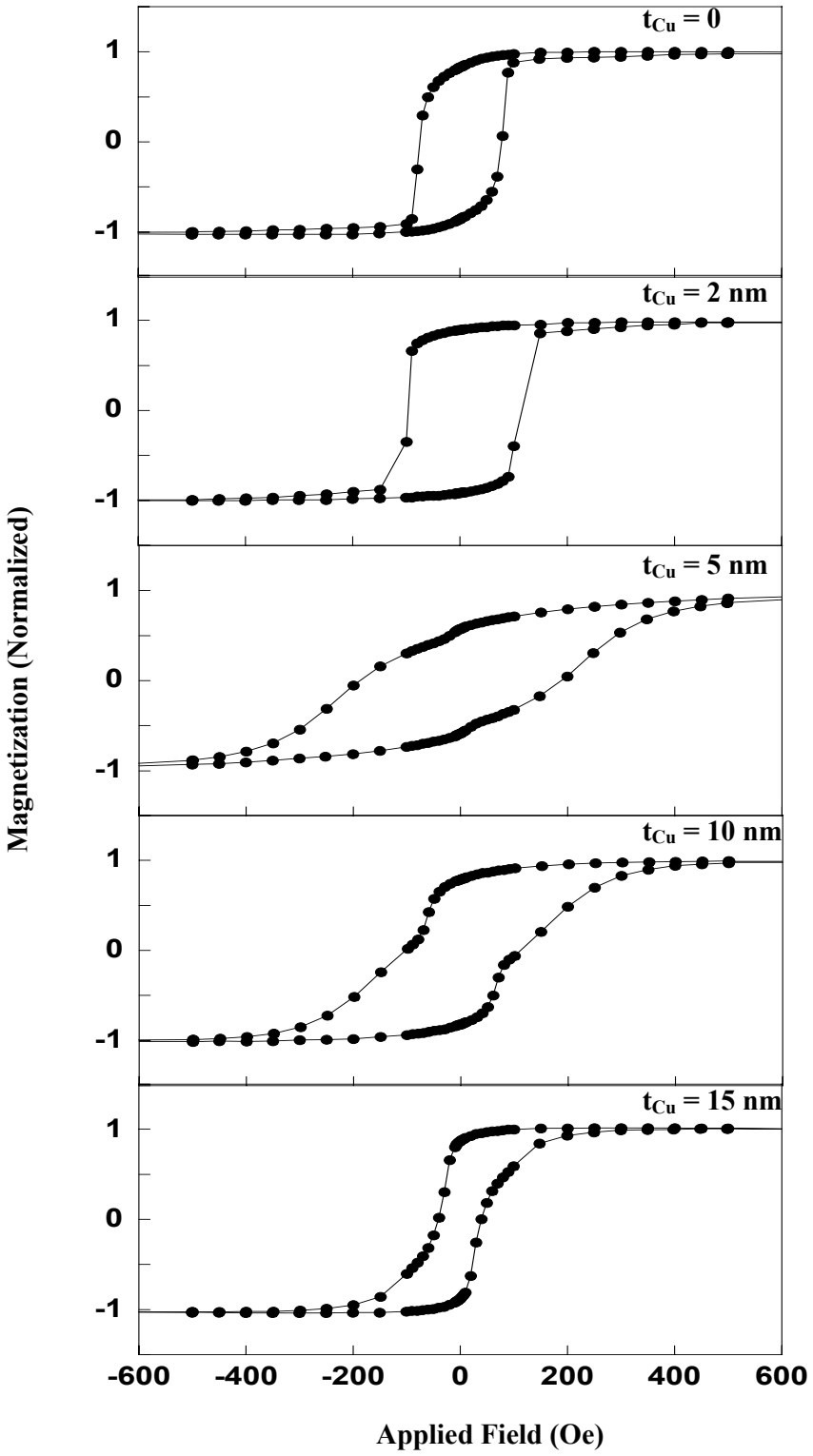


*Fig. 4.2 Magnetic Hysteresis loops for different Cu spacer layer thickness in [Co/Cu ($t_{Cu}$)/ Co]$_2$ multilayer structure*

We observed that the shape and detailed features of the M – H loops is strongly dependent on the Cu space layer thickness.

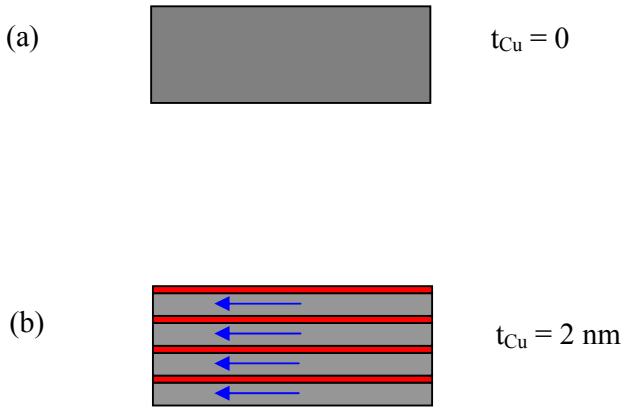


*Fig. 4.3 Detailed [Co/Cu ($t_{Cu}$)/ Co]$_2$ structure for (a) $t_{Cu} = 0$ and (b) $t_{Cu} = 2$ nm*

It is possible to explain the observed trend in the M – H loop by considering the type of coupling between ferromagnetic layers. Shown in Fig. 4.3 are sketches, illustrating the coupling mechanism for $t_{Cu} \leq 2$nm.

For $t_{Cu} \leq 2$nm, the interlayer exchange coupling between the ferromagnetic layers is very strong when compared with magnetostatic interaction which is long range. From the figure, the multilayer structure with $t_{Cu} = 2$ nm and that of Co single film ($t_{Cu} = 0$) were saturated at low fields with a large remanence $M_r$, close to the saturation magnetization $M_s$, indicating that the Co layer magnetic moments are aligned parallel in zero field and the interlayer coupling is ferromagnetic (FM).

Shown in Fig. 4.3 (c) is a schematic diagram illustrating the coupling mechanism between the ferromagnetic layers for $t_{Cu}$ = 5 nm.

(c) 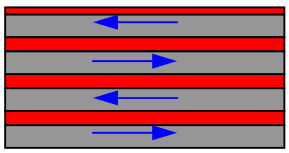 $t_{Cu}$ = 5 nm

*Fig. 4.3 (c) Related detailed structure for $t_{Cu}$ = 5 nm in [Co/Cu ($t_{Cu}$)/ Co]$_2$ structure*

For $t_{Cu} \geq 2$ nm, the interlayer exchange coupling is weak but the magnetostatic interaction between the magnetic layers via Cu spacer layer is stronger. This magnetostatic coupling helps in the stabilization of anti parallel relative alignment of magnetization in the adjacent magnetic layer at low fields, suggesting a strong anitiferromagnetic coupling between ferromagnetic layers.

Moreover, for $t_{Cu} \geq 5$ nm, we observed an onset of two step switching process which becomes pronounced as $t_{Cu}$ is increased as shown in Fig. 4.3. The magnetic layers are exchange decoupled. This corresponds to having individual 10 nm Co layers decoupled. The decrease in $H_c$ with increasing $t_{Cu}$ may be attributed to the thickness dependent of the coercivity. For $t_{Cu}$ = 0, the cobalt thickness is $t_{Co}$ = 40 nm. For $t_{Cu} \geq$ 10 nm, the cobalt thickness $t_{Co}$ = 10 nm.

To further analyze the effect of interlayer exchange coupling, we have extracted the coercivity, saturation field and film squareness from the M – H curves shown in Fig. (4.4).

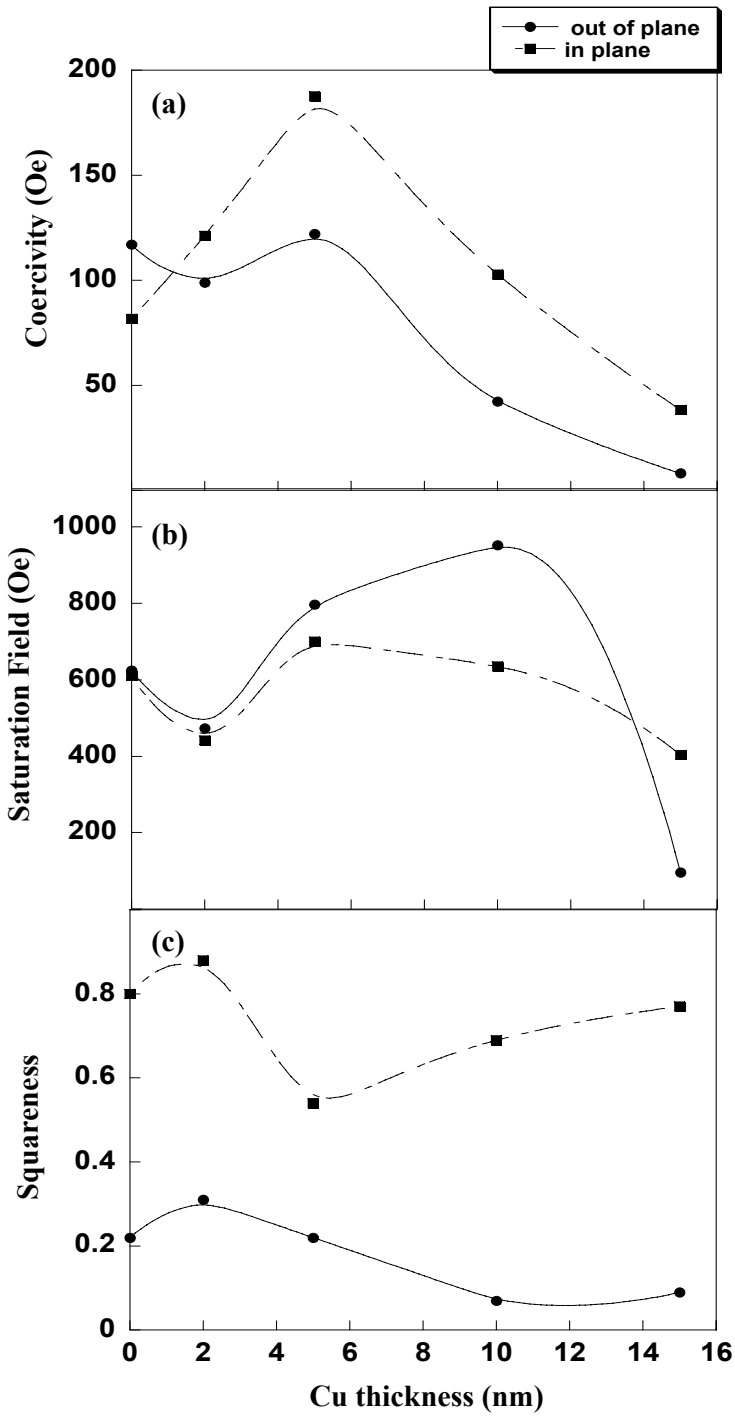


*Fig. 4.4 The comparison of (a) coercivity ($H_c$), (b) saturation field ($H_s$) and (c) squareness as a function of Cu spacer layer thickness in [Co (10 nm)/Cu ($t_{Cu}$)/Co (10 nm)]$_2$ multilayer structure for in plane and out of plane*

Shown in Fig. 4.4 (a) is a comparison plot of coercivity $H_c$ as a function of $t_{Cu}$ for in plane and out of plane. From the figure, we observed $H_c$ is very sensitive to the spacer layer thickness in Co/Cu multilayer films. As the Cu spacer layer film thickness increases, the coercivity value rapidly rises and reaches maximum value at $t_{Cu}$ = 5 nm due to the effect of exchange coupling between the layers. As $t_{Cu}$ is further increased, the $H_c$ value decreases. This is because exchange interaction between the layers is reduced. However, the layers are still coupled by magnetostatic interactions which support anti - parallel alignments at low fields.

Shown in Fig. 4.4 (b) and Fig. 4.4 (c) are the film squareness (S) and saturation field ($H_s$) – the minimum field required to align the magnetic domains in one direction - as a function of Cu thickness respectively. When $t_{Cu}$ = 2nm, the value of $H_s$ decreases as compared of the value of $H_s$ at $t_{Cu}$ = 0. This trend is because of the strong exchange coupling. For $t_{Cu}$ = 5 nm, the $H_s$ value reaches a maximum corresponding to maximum coercivity whereas the squareness value reaches a minimum.

For $t_{Cu}$ > 5 nm, there is a drastic decrease in the saturation field corresponding to an increase in the M – H loop squareness.

From the figures 4.4 (a) - 4.4 (c), we can see the same trends in the magnetic properties for both the in plane and out of plane components of magnetization in [Co (10 nm) /Cu ($t_{Cu}$) /Co (10 nm)]$_2$ structure.

## 4.5 Magnetotransport in Co / Cu/ Co Multilayer films

In order to fully understand the role of interlayer on the exchange coupling mechanism, magnetotransport measurements were carried out on the six terminal devices fabricated using shadow mask technique. Shown in Fig. 4.5 is a schematic diagram of the final device.

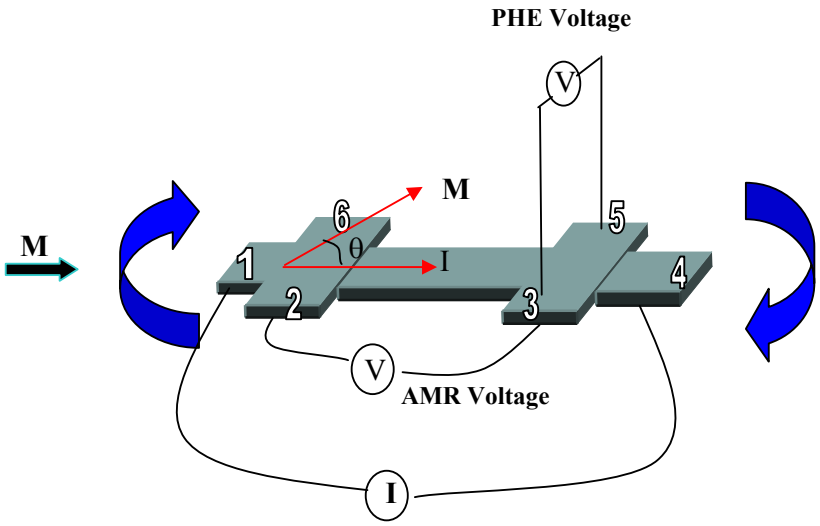


*Fig. 4.5 Electrical connections for AMR and PHE measurements*

A constant current (I) is passed through contacts (1) and (4) and the PHE ($V_{35}$) and AMR ($V_{23}$) are recorded simultaneously as the in – plane magnetic field was swept at constant rate.

All the data presented in this thesis are recorded at room temperature.

For PHE and MR measurements, a constant current of 1 mA was passed through contacts (1 & 4) shown in Fig 4.5 and the MR voltage ($V_{23}$) and PHE voltage ($V_{35}$) recorded simultaneously as the in – plane magnetic field was swept. We have probed the effects of interlayer exchange coupling in the multilayer by comparing the PHE and AMR outputs as a function of Cu spacer layer thickness in the range $0 \leq t_{Cu} \leq 10$ nm.

Shown in Fig. 4.6 are the representative AMR ($V_{23}$) and PHE ($V_{35}$) voltage responses to field applied along the sense current direction (i.e $\theta = 0°$) as a function of Cu spacer layer thickness.

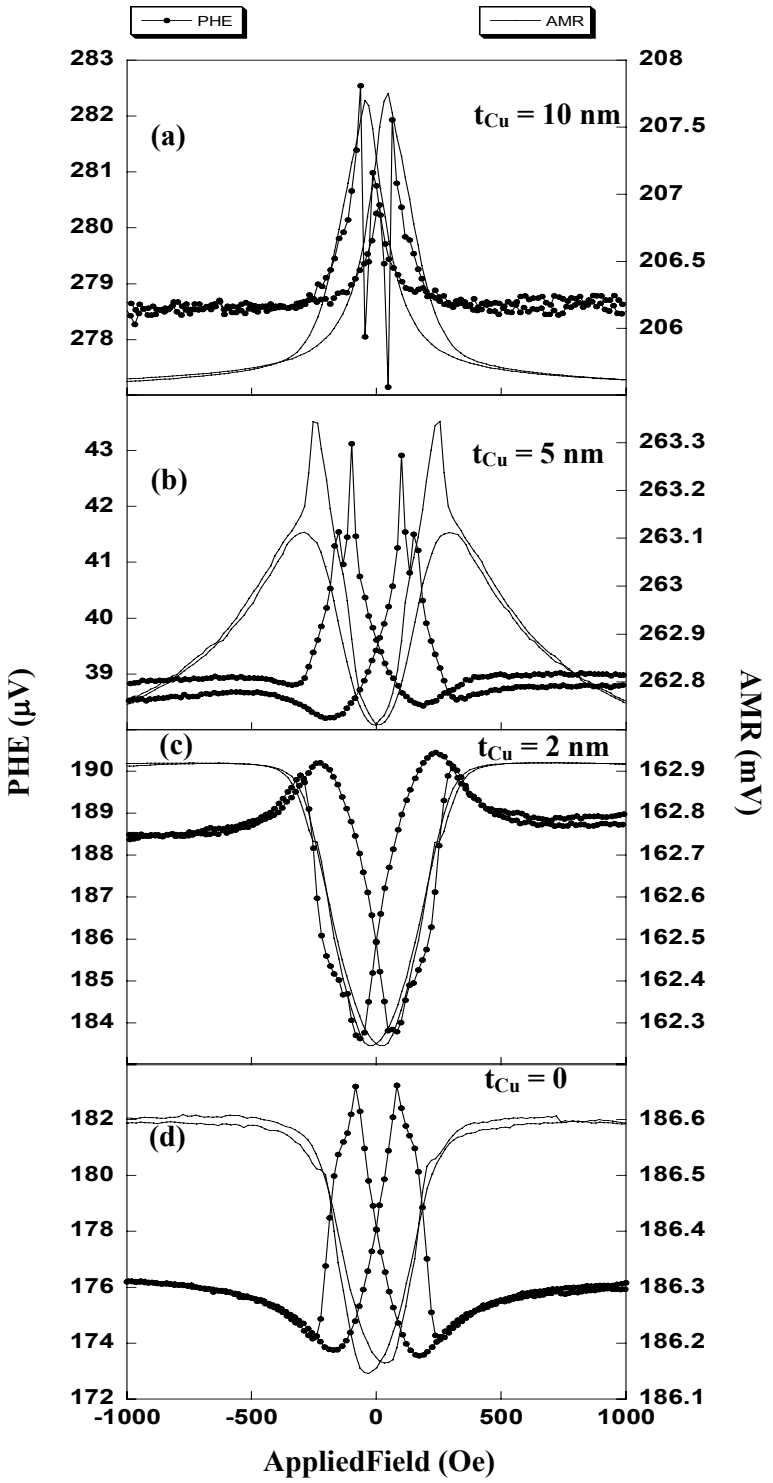


*Fig. 4.6 Planar Hall Effect (V35 – H) and AMR ($V_{23}$ – H) as a function of Cu spacer layer thickness for field applied along $\theta = 0°$*

Prior to the measurements, a field of ~1000 Oe was applied along the direction of sense current. This was sufficiently large so as to saturate the magnetization in the positive direction. The magnetic field was then swept back toward a negative value at constant rate and the corresponding $V_{35}$–H and $V_{23}$ – H forward loops were recorded automatically. The reverse $V_{35}$ – H and $V_{23}$ – H loops were obtained after applying a field H ~-1000 Oe and then sweeping H toward positive values.

We observed that both the AMR and PHE outputs are strongly dependent on the Cu spacer layer thickness.

For $t_{Cu} \geq 5$ nm, the PHE ($V_{35}$ – H) loops show multiple peaks in both the reverse and forward directions. The numbers of peaks are different at the different angles of applied field. We can see clearly that the PHE effect is sensitive to the magnetization in each layer constituting the multilayer films.

For $t_{Cu} \leq 2$ nm, the AMR output can readily be explained, because when the sense current and magnetization directions are co – linear, the resistance is maximum. At high field, this is what was observed was experimentally.

For $t_{Cu} \geq 5$ nm, however, a complex MR response was not readily explained by AMR model. At high field, for example, when the magnetization and sense current are collinear, the resistance is minimum.

This may be due to the fact that there is a combination of AMR and GMR effect to the observed response because of the anitiferromagnetic coupling which favours the GMR behaviour.

This result is in agreement with the M – H loop results presented in Fig. 4.2.

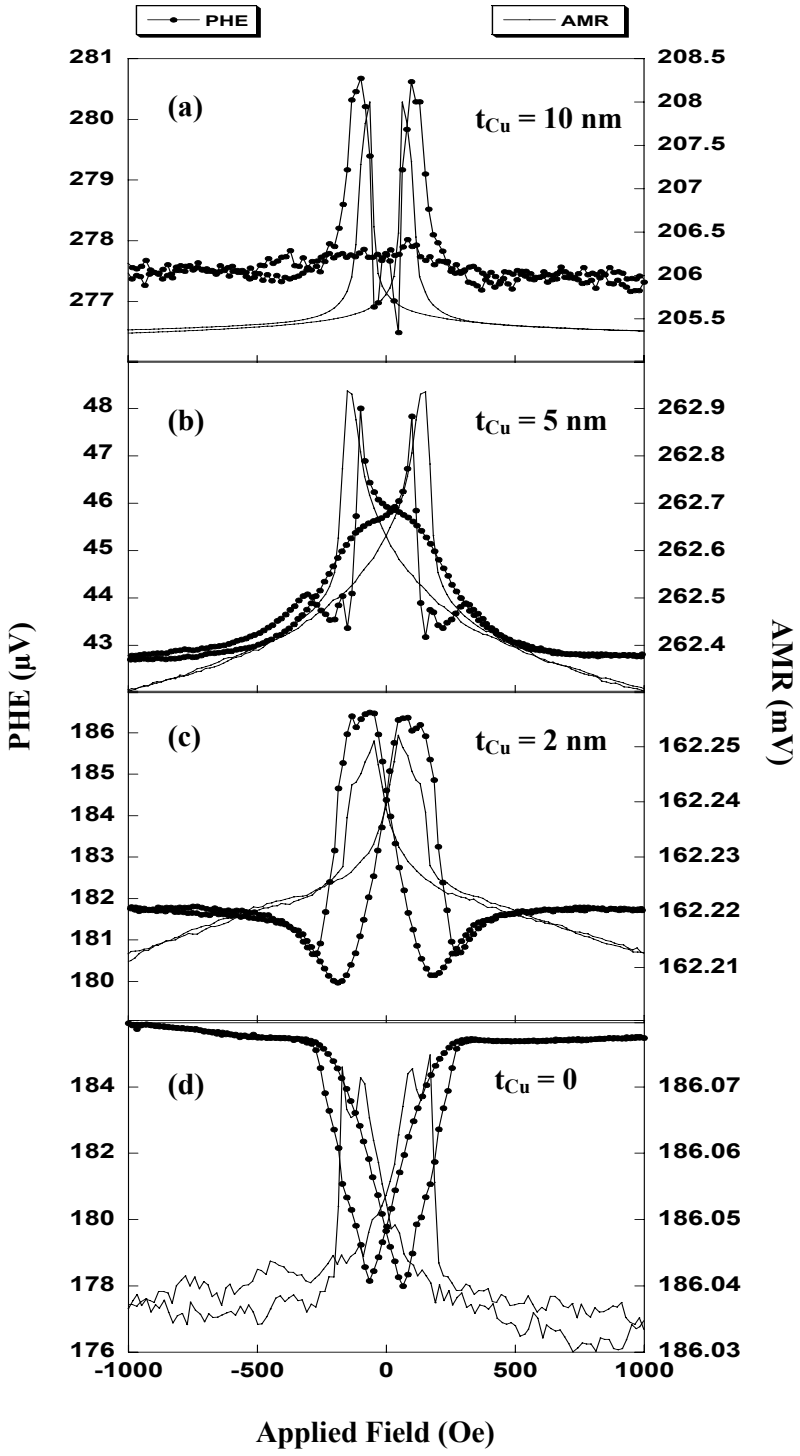


*Fig. 4.7 PHE ($V_{35}$ – H) and AMR ($V_{23}$ – H) as a function of Cu spacer layer thickness for field applied along $\theta = 90°$*

Shown in Fig. 4.7 (a) are the representative PHE ($V_{35}$ – H) and AMR ($V_{23}$ – H) outputs for Co/ Cu/ Co multilayer as a function of Cu interlayer thickness when the applied field is along the $\theta = 90°$ direction i.e the applied field is perpendicular to the direction of the sense current.

The sign of the AMR output voltages ($V_{23}$ – H) can be readily described by anisotropic magnetoresistance effect; i.e the resistance is minimum at high field when the magnetization is perpendicular to the direction of sense current.

The corresponding MR responses are also shown in Fig. 4.7. The MR response is found to be very sensitive to the spacer layer thickness. The largest MR ratio (%) was obtained when the Cu thickness $t_{Cu}$ = 10 nm. The MR ratio for $t_{cu}$ = 5nm is about 10 times higher than $t_{Cu}$ = 2nm. Since the drop in MR for thinner Cu is mainly due to an increase in ferromagnetic coupling between the layers, the agreement in that part of the curve implies a similar Cu result for $t_{Cu} \leq 2$ nm [5]. The field ($H_s$) at which the sharp peaks occur in the MR curves corresponds to the switching of magnetization and is found to be dependent on the Cu spacer layer thickness.

The slope and sign of PHE output voltage ($V_{35}$ – H) is strongly dependent on the spacer layer thickness and characterized by multiple jumps in both the forward and reverse directions. The transition from ferromagnetic (FM) to antiferromagnetic (AFM) coupling can readily be seen when the comparison of PHE output for $t_{Cu}$ = 2 nm and 5 nm.

### 4.5.1 Comparison of PHE and MR as a Function of Field Orientation

In order to compare the sensitivity and angular dependence of PHE and MR output, we have carried out systematic measurements. Referring to the device geometry in Fig. 4.5, a sense current of 1 mA was applied to the device via current leads (1 & 4), then both AMR and PHE voltages were detected simultaneously by means of voltage leads (2 & 3) and (3 & 5) respectively.

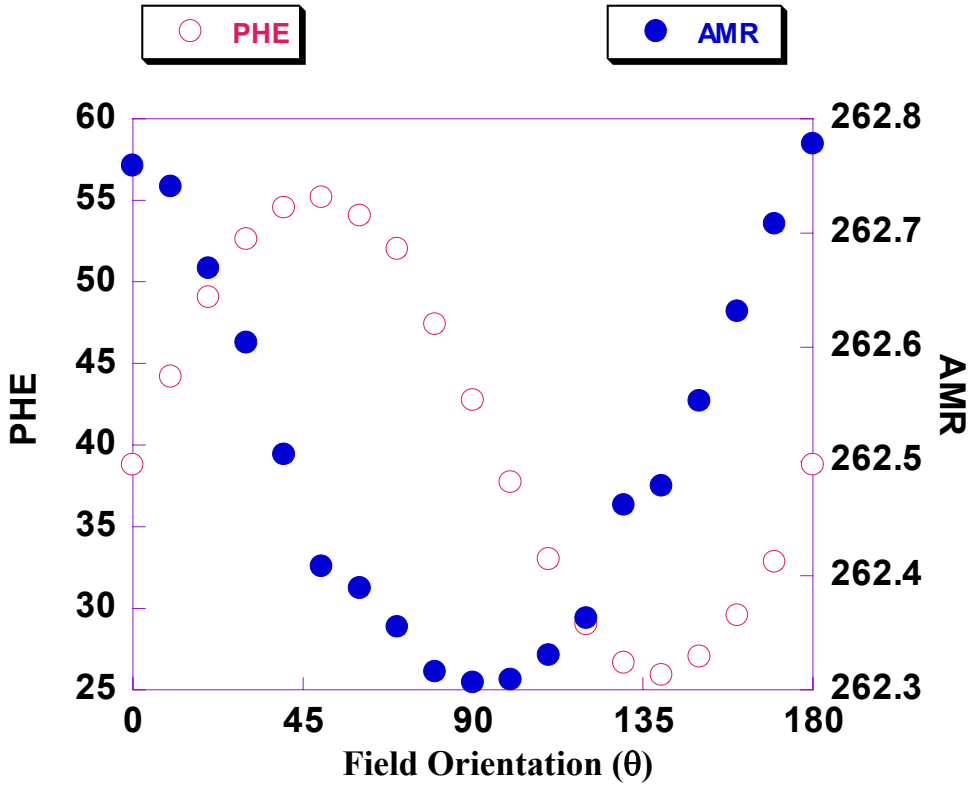


*Fig. 4.8 Direct comparison of PHE and MR output voltage for [Co (10nm) /Cu (5nm)/Co (10nm)]$_2$ multilayer.*

The magnitude of the applied field was kept constant during the measurements while the device was rotated in the applied field. In this case H=1000 Oe, strong enough to saturate the magnetization of the device was applied and the current I=1 mA. As

expected the dependence of $V_{23}$ on θ is of the form $V_{23} = Vo_{23} + \Delta Vo_{23}\cos 2\theta$. This can be attributed to the anisotropic magnetoresistance effect.

From Fig. 4.8, we can estimate $Vo_{23} = 262.51$ mV and $\Delta Vo_{23} = 0.15$ mV. We then calculate $\frac{\Delta Vo_{23}}{Vo_{23}}\% = 0.0572\%$. The dependence of $V_{35}$ on θ is however of the form $V_{35} = Vo_{35} + \Delta Vo_{35}\sin 2\theta$. We have estimated $Vo_{35} = 38.80$ μV and $\Delta Vo_{35} = 15.74$ μV from Fig. 4.8. The value of $\frac{\Delta Vo_{35}}{Vo_{35}}\% = 40.56\%$. This result is in agreement with Kakuno's results [12]. Moreover, a 45° shift was observed between the AMR and PHE curves. This is also in agreement with the theoretical prediction (see Eqn 2.3 and Eqn. 2.4)

### 4.5.2 PHE voltages as a function of orientation of applied field

Shown in Fig. 4.9 is the PHE output voltage $V_{35}$ as a function of orientation (θ) of the applied field relative to direction of the sense current for [Co (10 nm)/ Cu ($t_{Cu}$) / Co (10 nm))$_2$ multilayer as a function of Cu thickness. For each of the angular dependence plots, the magnitude of the applied field was kept constant at H =100 Oe, 200 Oe and 1000 Oe, while the device was rotated from 0° to 180° and the voltage $V_{35}$ recorded at 10° intervals.

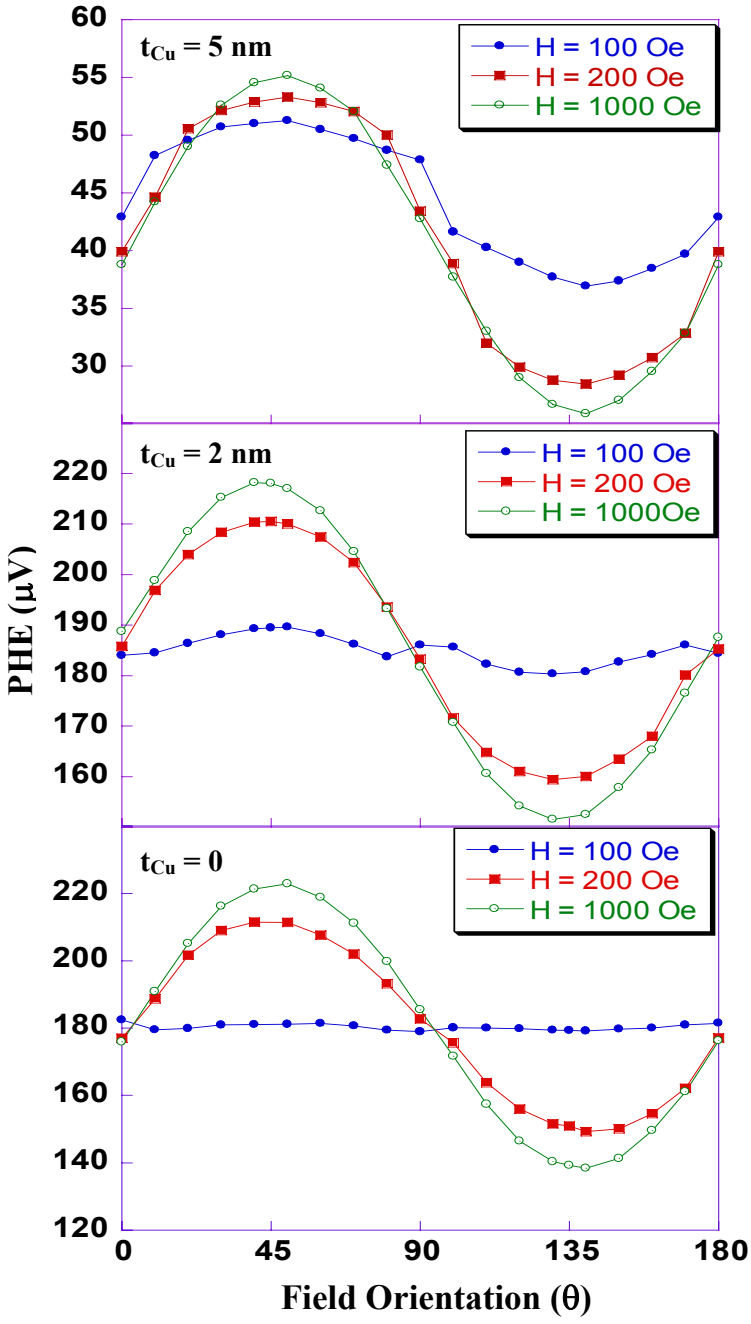


*Fig. 4.9 PHE voltages as a function of applied field relative to the direction of the sense current for [Co (10 nm)/Cu ($t_{Cu}$) /Co (10 nm)]$_2$ multilayer as a function of Cu thickness*

We observed for all the $t_{cu}$ that when the applied field H ≥ 1000 Oe, there is a Sin2θ dependence in the PHE output Voltage as a function of θ. This can be attributed to the fact that the magnitude of the applied field is greater than the saturation field of the films and is in agreement of theoretical predictions.

For H = 200 Oe, however, we observed a drop in the PHE output voltage, due to the fact that all the spins are not fully saturated. When H ≤100 Oe, a drastic drop in the PHE output voltage and a departure from the sin2θ dependent was observed for $t_{Cu}$ = 2 nm and 0. Hence domain wall activities prevail. This shows that PHE output voltage is very sensitive to the exact spin state.

### 4.5.3 AMR voltages as a function of orientation of applied field

Shown in Fig. 4.10 is the AMR output voltages $V_{23}$ as the function of orientation (θ) of the applied field relative to direction of the sense current for [Co ( 10 nm)/Cu($t_{Cu}$) /Co (10 nm)]$_2$ as a function of Cu thickness. For all angular dependence plots, the field was kept constant at 100 Oe, 200 Oe and 1000 Oe while the device was rotated from 0° to 180° and the AMR output voltages ($V_{23}$) were recorded each 10 ° interval.

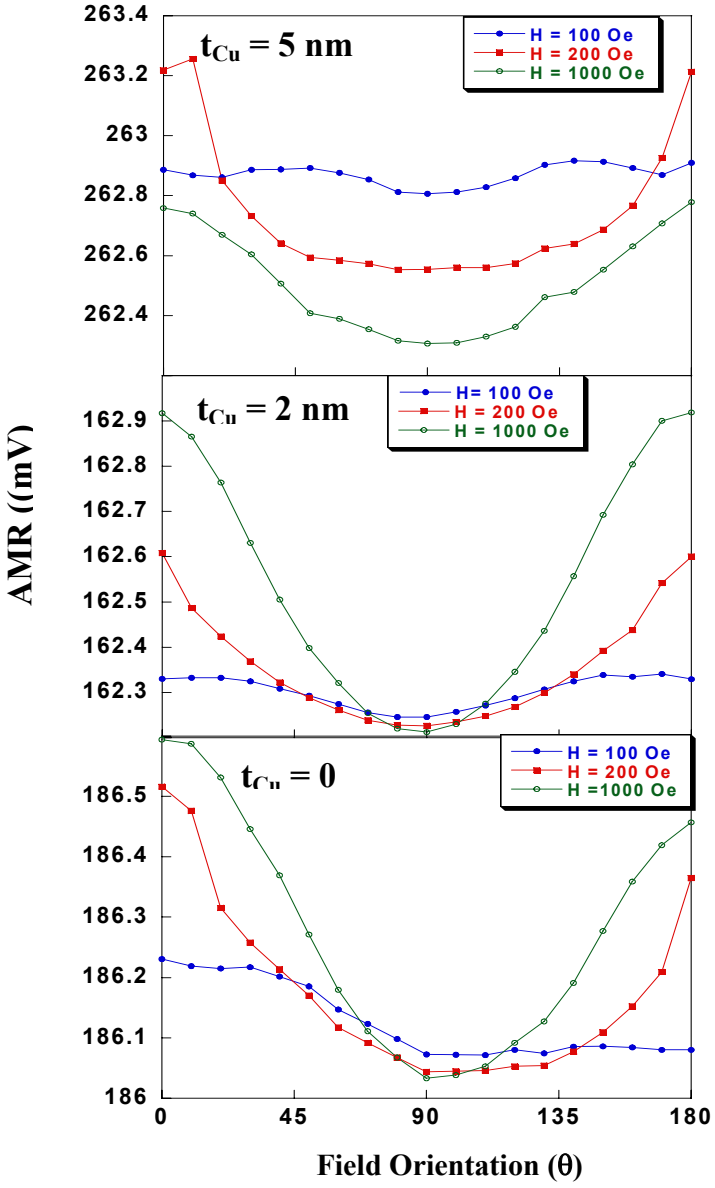


*Fig. 4.10 AMR output voltage ($V_{23}$) as a function of field orientation relative to the direction of sense current in [Co (10 nm)/Cu ($t_{Cu}$) / Co (10 nm)] multilayer structure for various $t_{Cu}$*

We observed a departure from the $\cos^2 \theta$ predicted by anisotropic magnetoresistance model when the applied field $H \leq H_s$. This is caused by domain wall propagation. This is an agreement with the theoretical prediction from $H \geq H_s$, where $H_s$ is the saturation field.

## 4.6 PHE and AMR effects in [NiFe (10nm)/ Cu ($t_{Cu}$)/ NiFe (10nm)]$_2$ multialyer

We have also investigated the PHE and AMR effects in NiFe/ Cu/ NiFe multilayer. The devices were fabricated using shadow mask technique described in Section 4.2. Shown in Fig. 4.11 is a direct comparison of both AMR and PHE outputs in NiFe (10 nm)/ Cu ($t_{Cu}$) / NiFe (10 nm) multilayer as a function of Cu layer thickness. Again, we observed that the PHE output is very sensitive to the interlayer thickness.

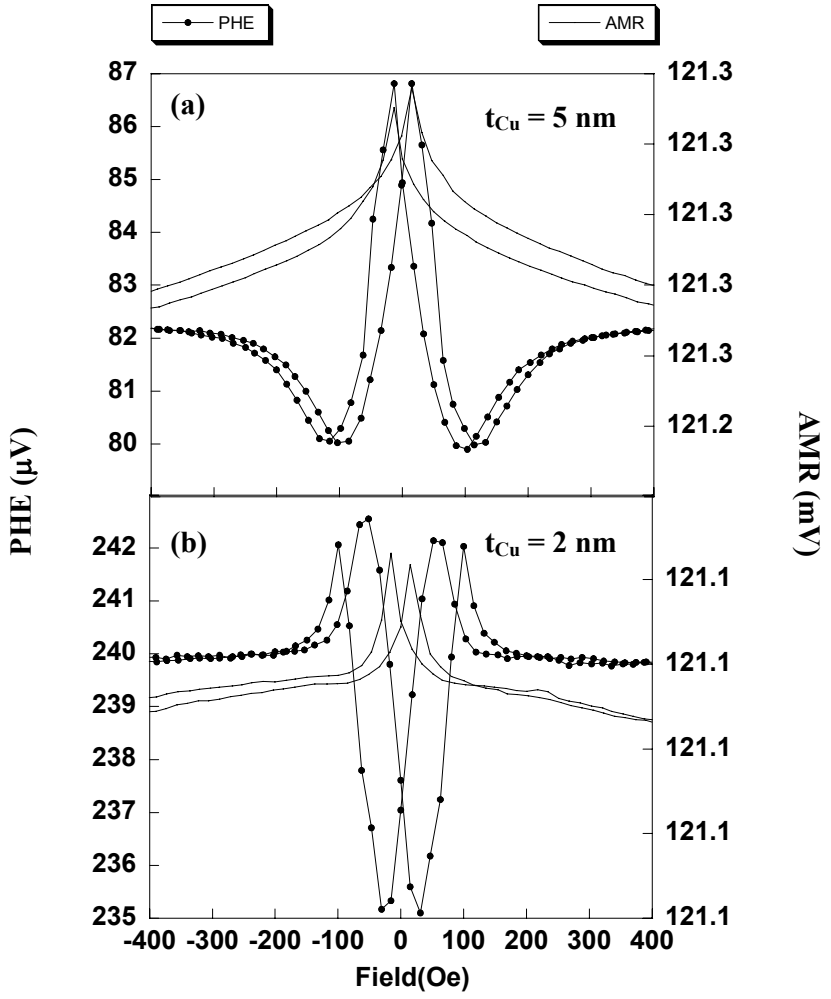


*Fig. 4.11 Comparison of PHE and MR results as a function of Cu spacer layer thickness in [NiFe (10nm)/ Cu ($t_{Cu}$)/ NiFe (10 nm)]$_2$ structure for 90 field orientation*

Shown in Fig. 4.12 are the representative angular dependent AMR and PHE outputs for [NiFe (10 nm)/ Cu (5 nm)/ NiFe (10 nm)]$_2$ multilayer.

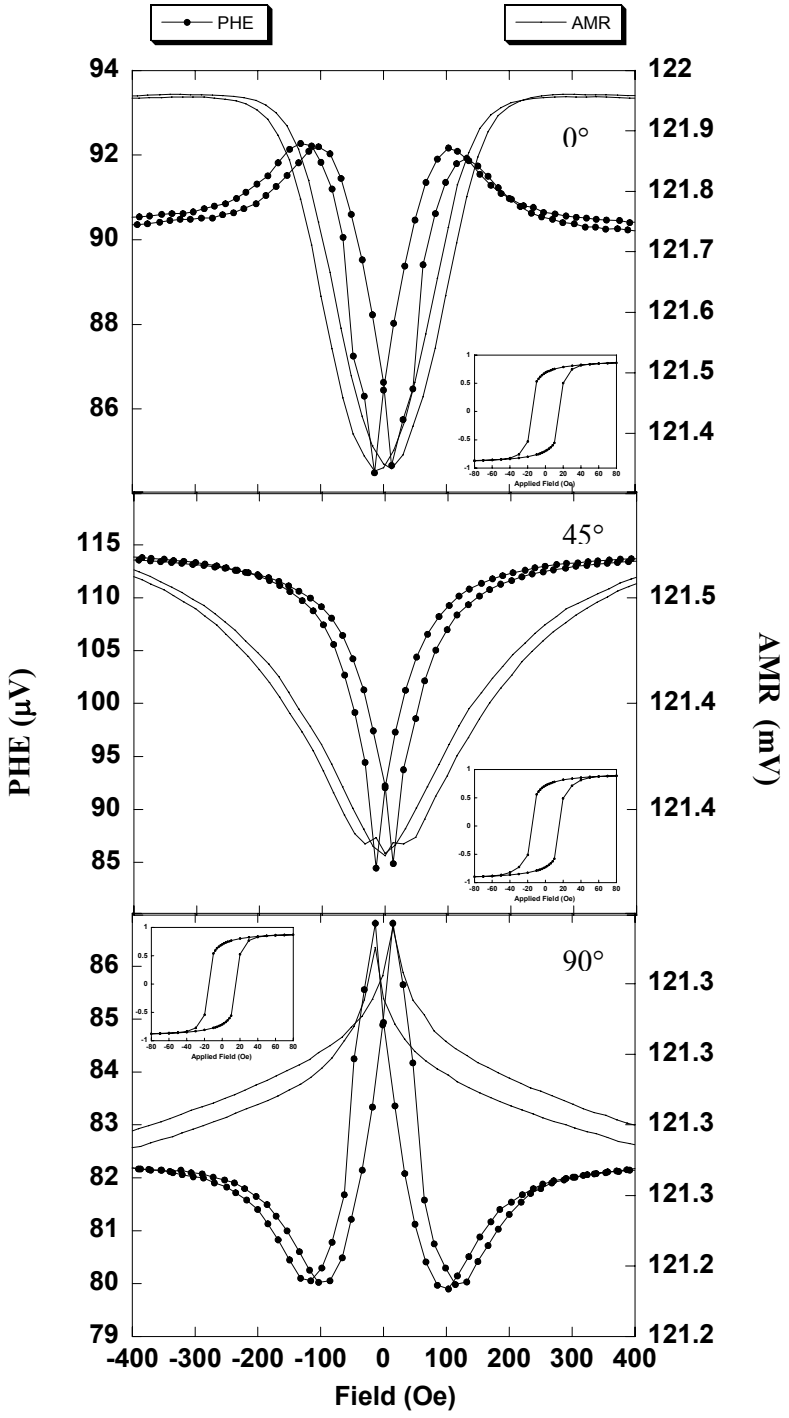


*Fig. 4.12 PHE and AMR output voltages for [NiFe (10 nm)/ Cu (5 nm)/ NiFe (10nm)]$_2$ multilayer structure with different field orientations*

## 4.7 Summary

We have investigated the effect of interlayer exchange coupling in [Co (10nm) /Cu ($t_{Cu}$)/Co (10nm)]$_2$ and [NiFe (10nm)/Cu ($t_{Cu}$)/ NiFe (10 nm)]$_2$ multilayers using a combination of planar Hall effects (PHE), anisotropic magnetoresistance measurements (AMR) and M – H loops. We made a direct comparison of AMR and PHE voltages as a function of the orientation of the constant applied field relative to the current direction. We observed a Sin2θ dependence on the PHE output when the applied field (H) is greater than the switching field ($H_s$) of the device, in agreement with theoretical prediction. For fields $H<H_s$, a departure from the sin2θ dependent was observed due to domain wall propagation. From the comparison of AMR and PHE, we can conclude that PHE gives better information in each layer.

**Reference:**

[1] M.N. Baibich, J.M. Broto, A.Fert, F.Nguyen Van Dau, F. Petroff, J. *Phys. Rev. Lett.* 61, 2472 (1988)

[2] F.Petroff, A. Barthelamy, D.H.Mosca, D.K.Lottis, A.Fert, P.A. Schroeder, W.P.

[3] S.S.P.Parkin, N.More and K.P.Koche, *Phys. Rev. Lett*. 64, 2304 (1990)

Pratt Jr., and R. Loloee, *Phys. Rev. B* (44), 5355 (1991)

[4] P. Grunberg, R. Schreiber, Y.Pang, M.B. Brodsky, and H. Sowers, *Phys. Rev. Lett.* 57, 2442 (1986).

[5] J.J. Krebs, P. Lubitz, A. Chaiken, and G.A. Prinz, *Phys. Rev. Lett*, 63, 1645 (1989).

[6] J.Unguris, R.J. Celotta and D.T. Pierce, *Phys. Rev. Lett*, 67, 140 (1991).

[7] Q.Y.Jin, H.R.Zhai, Y.B.Xu, Y.Zhai, M.Lu, S.M.Zhou, J.S.Payson, G.L. Dunifer, R.Naik, G.W.Auner, *J.Appl.Phys*. 77 (8), 15 April 1995

[8] S. Honda, T.Mimura, S. Ohmoto and M. Nawate, *IEEE. Trans. Magn*, Vol.28, No.5, September 1992

[9] Shan X. Wang and Alexander M. Taratorin, *Magnetic Information Storage Technology*, (1999), Academic Press.

[10] A.Schuhl, F. Nguyen Van Dau, and J.R.Childress, *Appl. Phys. Lett*. 66 (20) 1995

[11] Ilsu and Chan Kim, *IEEE. Trans. Magn*, Vol. 37, No 2, March 2001

[12] K. Kakuno, Japn. *J. Appl. Phys*., 30 (11A), 2761 (1991).

# Chapter 5

# Finite Size Effects of Magneto Transport Properties in Multilayer Structures

## 5.1 Overview

In this chapter, we present the results of our investigations in the role of finite size on the magnetic properties of multilayer films and the interlayer exchange coupling. The samples were fabricated by electron beam and optical lithography, deposition and lift off methods.

## 5.2 Experimental Procedure and Measurement Set up

In the first experimental batch, magnetic multilayer based planar hall devices were fabricated on Si (100) using photolithographic process. The substrates were fabricated on an undoped Si wafer. The widths of the devices were varied in the range 7 μm to 40 μm.

The deposition of the magnetic multilayer conditions is listed in Table 5.1.

| Materials | Deposition System | Deposition Rate |
|---|---|---|
| Co | E beam evaporation | 0.5 Å/sec |
| Cu | Thermal evaporation | 0.2 Å/sec |
| NiFe | E beam evaporation | 0.3 Å/sec |
| Al | DC sputtering | 1.2 Å/sec |

*Table 5.1 The parameters for the deposition of Co, Cu, Al and NiFe materials*

A typical configuration for the measurements of PHE and AMR voltages is illustrated as Fig. 5.1.

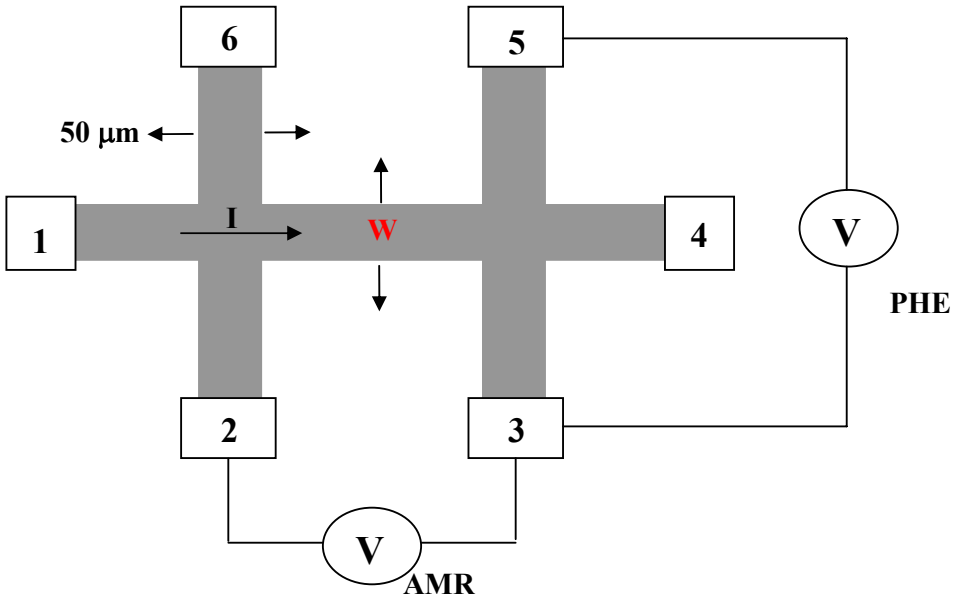


W = 7, 15, 20 and 40 μm

*Fig. 5.1 Schematic representation of the device geometry with external contacts*

## 5.3 Theory

If the magnetic materials has finite length the generation of 'magnetic poles' near its ends gives rise to a magnetic field opposing the applied field. This opposing field is called the demagnetizing field. The strength of the demagnetizing field depends on two factors only. These are the magnetization in the material (i.e the pole strength) and the shape of the specimen (i.e the pole separation which is determined by sample geometry). Demagnetization field plays an important role in determining the devices performances.

The demagnetizing field is proportional to the magnetization and is given by the expression [1]

$$\mathbf{H_d} = - N_d \mathbf{M} \text{ ……..Eqn 5.1}$$

where $N_d$ is a demagnetizing factor which is calculated solely from the sample geometry.

In this chapter where the device width was varied, the $H_d$ associated along the width dimension is expected to vary too.

## 5.4 Results and Analysis

### 5.4.1 Experimental Results and Analysis for [Co (10 nm)/ Cu ($t_{Cu}$) / Co (10 nm)]$_2$ Multilayer Structures

In this section, the role of size effects and the effects of Cu spacer layer thickness on [Co (10 nm)/ Cu ($t_{Cu}$) / Co (10 nm)]$_2$ multilayer structures are investigated.

A constant current of 1 mA was applied through the contacts 1 and 4 (shown in Fig 5.1). PHE ($V_{35}$) and AMR ($V_{23}$) voltages were recorded at every 15º intervals.

In order to investigate the effect of pattern size widths in [Co (10 nm)/ Cu (5 nm)/ Co (10 nm)]$_2$ multilayer using PHE and AMR , we have measured PHE – H and AMR – H loops for various widths.

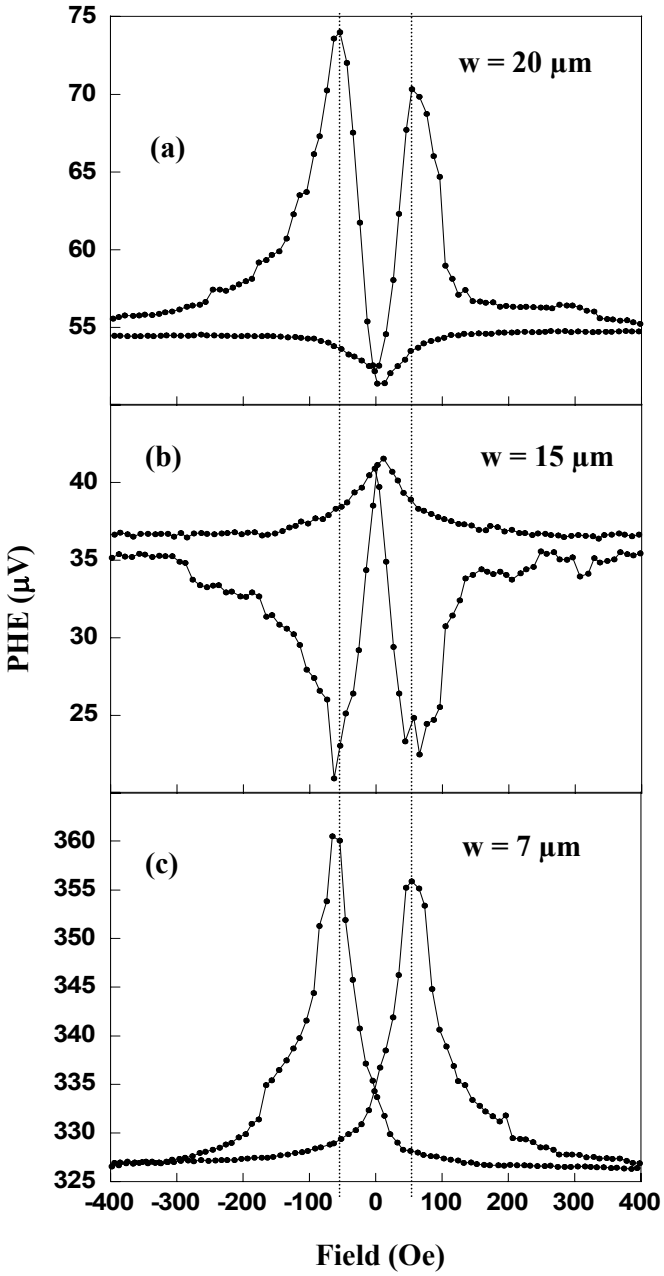


*Fig. 5.2 PHE results as a function of different widths in [Co (10nm)/ Cu (5 nm)/ Co (10 nm)]$_2$ multilayer structures*

Shown in Fig (5.2) are PHE responses to field applied perpendicular ($\theta = 90°$) to the sense current as a function of device widths for [Co (10nm)/ Cu (5 nm)/ Co (10nm)]$_2$ multilayer structure.

We observe that both the shape and sign of the PHE curves are strongly size dependent.

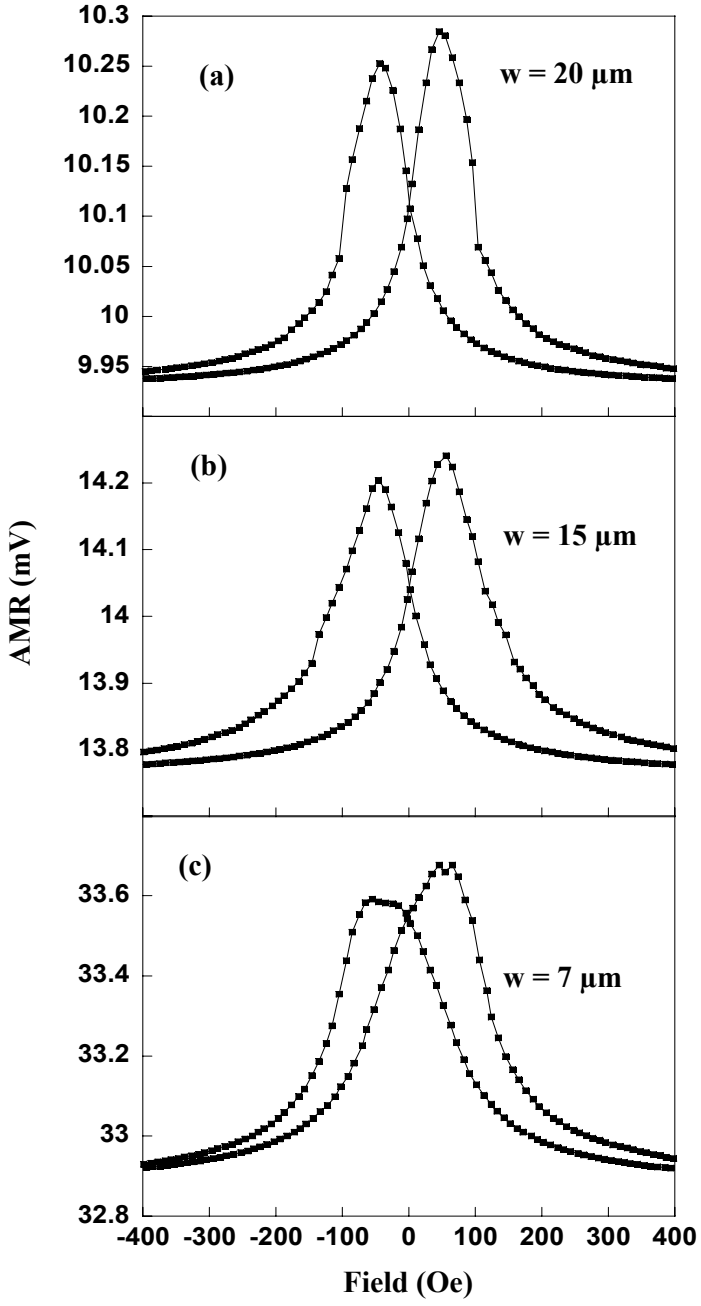


*Fig. 5.3 Comparison of AMR output voltages for different size widths in [Co (10nm)/ Cu (5 nm)/ Co (10 nm)]$_2$ multilayer structure*

The corresponding AMR response to field applied perpendicular to the sense current is shown in Fig. 5.3. While the sign of the AMR response are identical, there are marked changes in the detailed features due to finite size effect.

The MR was measured at room temperature and the MR% was defined as follows:

$$MR\% = \frac{R(H_s) - R(H)}{R(H_s)} * 100 \quad \text{----------Eqn 5.2}$$

where R (H) and R ($H_s$) are the resistance measured at field H and saturation field ($H_s$).

| Width | MR% |
|---|---|
| 7 | 2.42 |
| 15 | 3.49 |
| 20 | 3.61 |

*Table 5.2 Compilation of AMR measurement for the field perpendicular to current direction*

From Table 5.2, we observed that the MR ratio depends on the width of the PHE device. When the size width decreases, the MR ratio also decreases, due to the surface scattering from the device edges.

Next, we investigate the effects of Cu spacer layer thickness on PHE and AMR measurements in [Co (10 nm)/ Cu ($t_{Cu}$)/ Co (10 nm)]$_2$ multilayer structure. The device width was fixed at w = 20 μm, while the Cu spacer layer thickness was varied from 2 to 10 nm.

Shown in Fig. 5.4 are the representatives of PHE output voltages as a function of Cu inter layer thickness. For $t_{Cu}$ = 10 nm, the loop is characterized by multiple jumps in both the forward and reverse field sweeps.

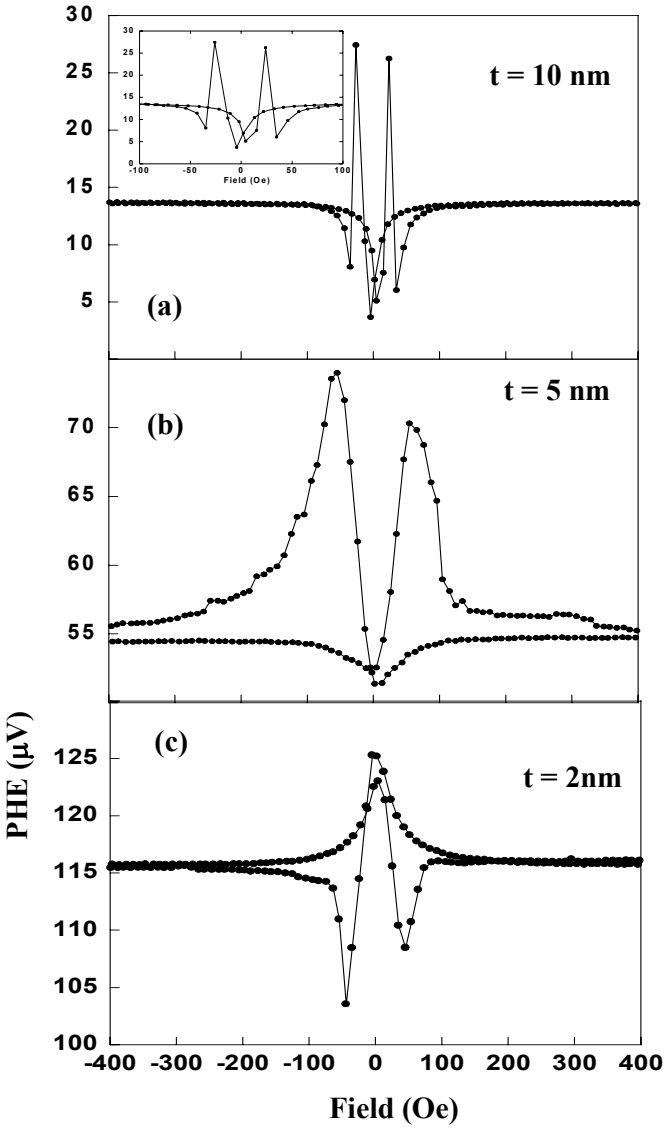


*Fig. 5.4 PHE output as a function of Cu spacer layer thickness for [Co (10 nm)/Cu ($t_{Cu}$)/ Co (10 nm)]$_2$ multilayer films with device width = 20 μm*

Shown in Fig. 5.5 are the corresponding AMR responses as a function of Cu inter layer thickness.

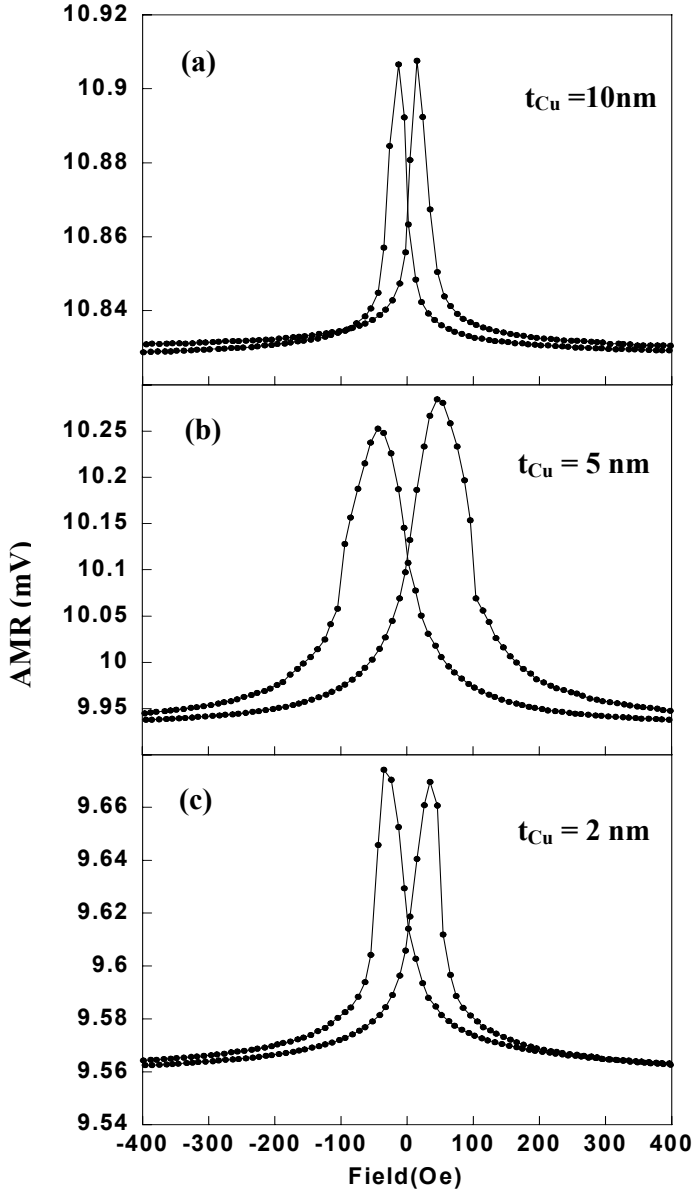


*Fig. 5.5 Comparison of AMR output voltages for different Cu spacer layer thickness for [Co (10nm)/ Cu ($t_{Cu}$)/ Co (10 nm)]$_2$ multilayer structure with device width 20$\mu$m*

## 5.4.2 Field Orientations effect on PHE and AMR results

In order to understand the field orientation dependent response for both PHE and AMR, the device with w = 20 μm for [Co (10nm)/ Cu (10 nm)/ Co (10 nm)]$_2$ multilayer structure was rotated in the plane of the magnetic field at a constant rate.

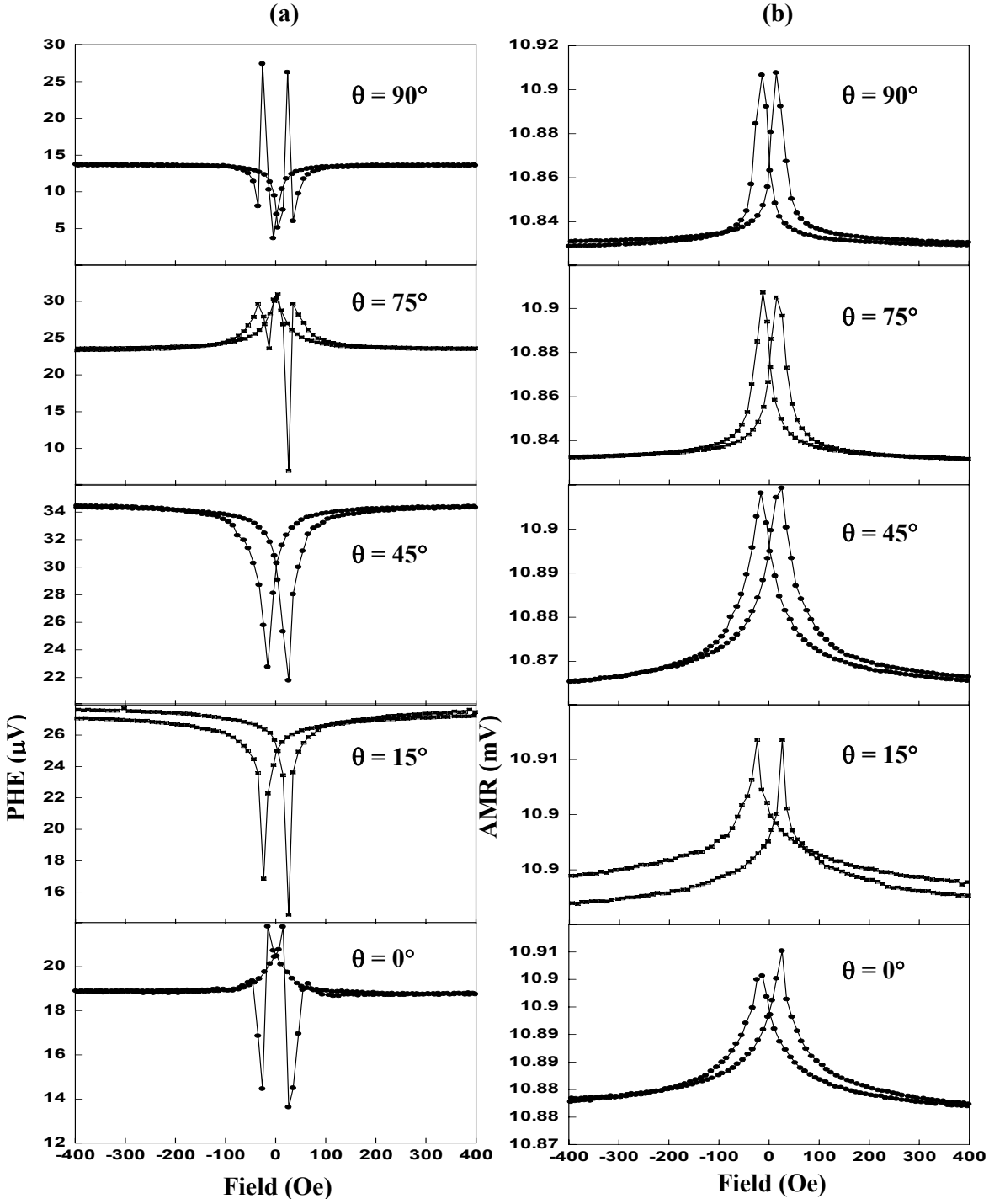


*Fig 5.6 PHE and AMR output voltages as a function of the orientation of applied field relative to the current direction for (10nm)/ Cu (10 nm)/ Co (10 nm)]$_2$ film*

Shown in Fig 5.6 are the representatives PHE and AMR loops as a function of the orientation of applied field (θ) in [Co (10nm)/ Cu (10 nm)/ Co (10 nm)]$_2$ multilayer structure.

It was seen that the signal of the planar Hall voltage is very sensitive to field orientationθ. The PHE curves show changes in the magnetization of each layer more sensitively as manifested by the observation of multiple peaks.

In order to compare the magnetic properties of films deposited by sputtering and electron beam technique, we have investigated the interlayer exchange coupling on film deposition using electron beam deposition. Shown in Fig 5.7 are the representative VSM hysteresis loops as a function of Cu interlayer thickness.

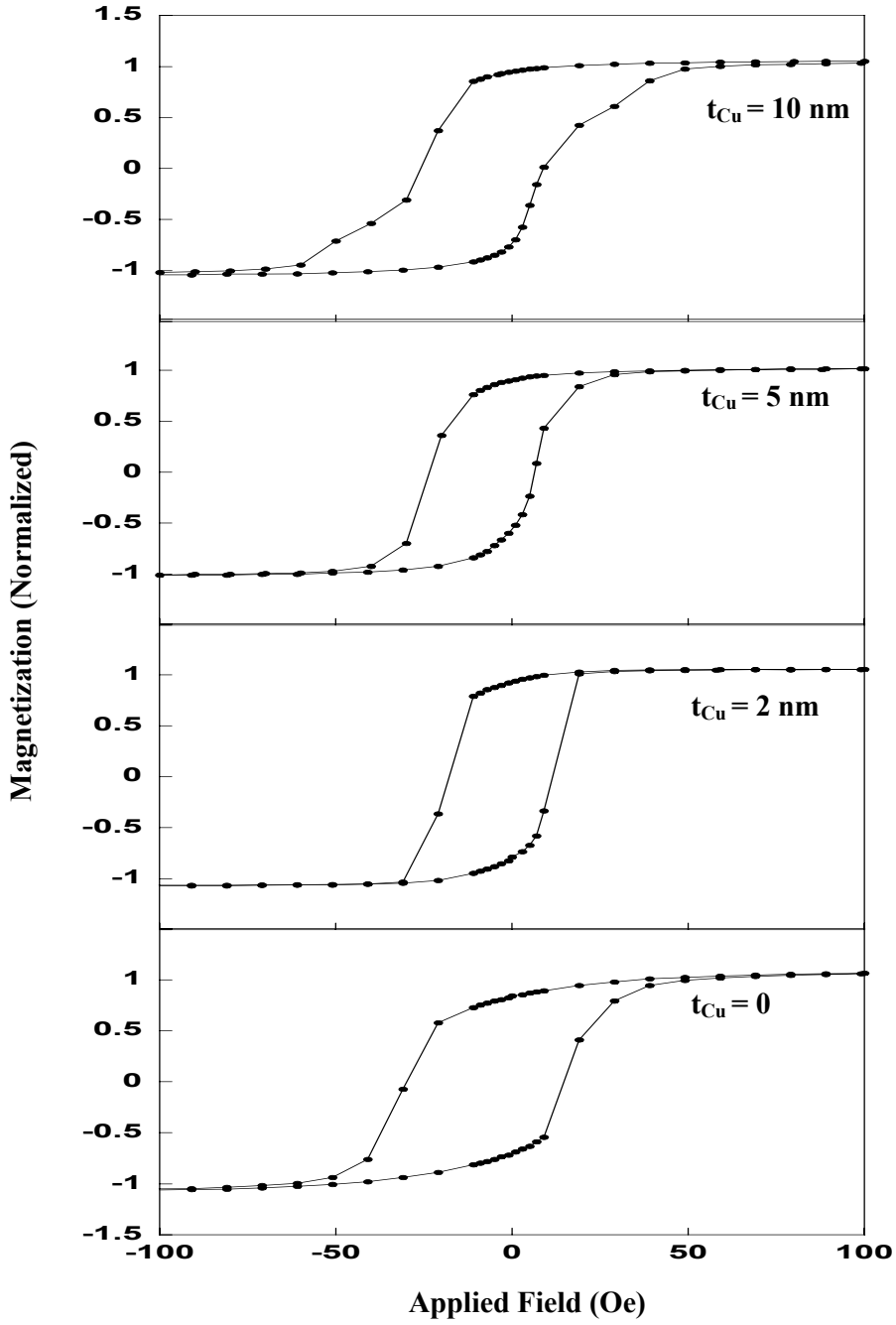


*Fig 5.7 Hysteresis loops as a function of Cu spacer layer thickness in [Co (10 nm)/ Cu ($t_{Cu}$) / Co (10 nm)]$_2$ multilayer structures*

The magnetic properties are sharply dependent on the Cu spacer layer thickness following the same trend with film deposited using sputtering in section 4.4.

A direct comparison between the sputtering and e beam deposition samples shows that the detailed features are different.

### 5.4.3 Experimental Results and Analysis for [NiFe (10nm)/ Cu ($t_{Cu}$)/ NiFe 10 nm)]$_2$ Multilayer Structure

In this section, we have investigated the magneto transport properties and magnetic properties for [NiFe (10nm)/ Cu ($t_{Cu}$)/ NiFe 10 nm)]$_2$ multilayer structure as a function of Cu spacer layer thickness.

These devices were fabricated using the method outlined in section 5.3 but NiFe material was deposited by e beam evaporation instead of Co material. There were 3 devices with different Cu spacer layer thickness ($t_{Cu}$ = 0, 5 and 10 nm).

A constant current of 1 mA was applied through the contacts 1 to 4 and the PHE ($V_{35}$) and the AMR ($V_{23}$) are recorded every 15° interval.

We have investigated the transport properties as a function of Cu interlayer spacing for various device widths. Shown in Fig 5.8 are the representative PHE and AMR plots as a function of Cu thickness for a [NiFe (10 nm)/ Cu (10 nm)/ NiFe (10 nm)]$_2$ structure.

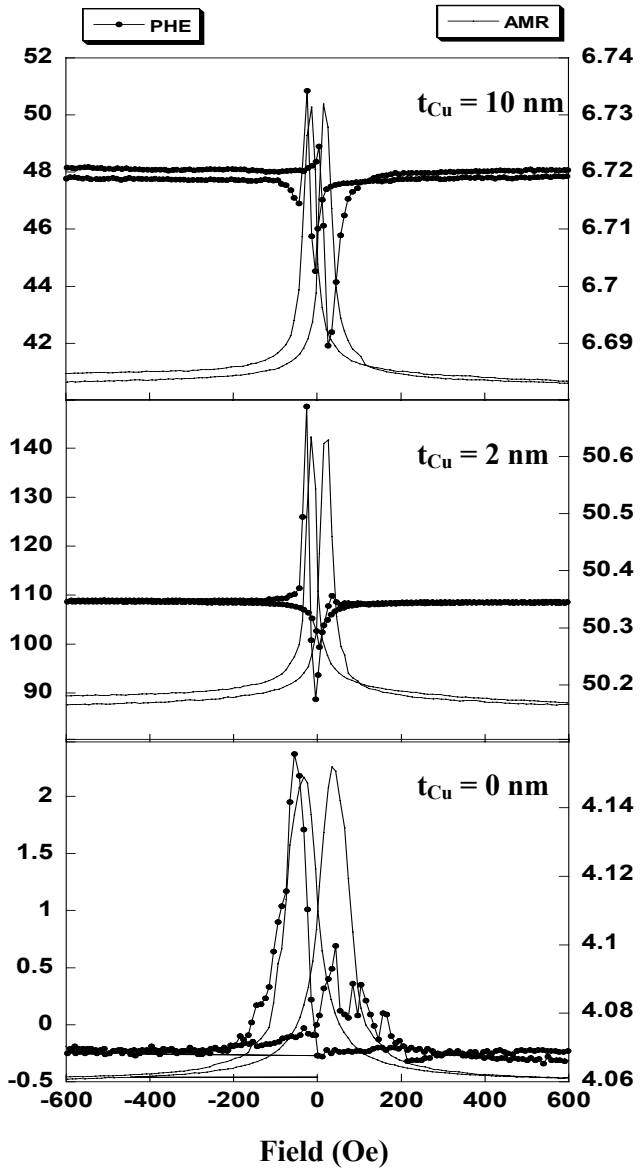


*Fig 5.8 PHE and AMR output voltages for [NiFe (10nm)/ Cu ($t_{Cu}$)/ NiFe 10 nm)]$_2$ multilayer structure as a function of Cu spacer layer thickness when the applied field is perpendicular to the sense current direction*

We observed that the devices switches at low field as expected because NiFe has low intrinsic magnetic anisotropy.

In order to investigate the magnetic properties in [NiFe (10 nm)/ Cu ($t_{Cu}$)/ NiFe (10 nm)]$_2$ multilayer structure as a function of Cu spacer layer thickness, the reference samples were prepared using thermal and e – beam evaporation. The vibrating sample magnetometer was used to measure the magnetic properties of these samples.

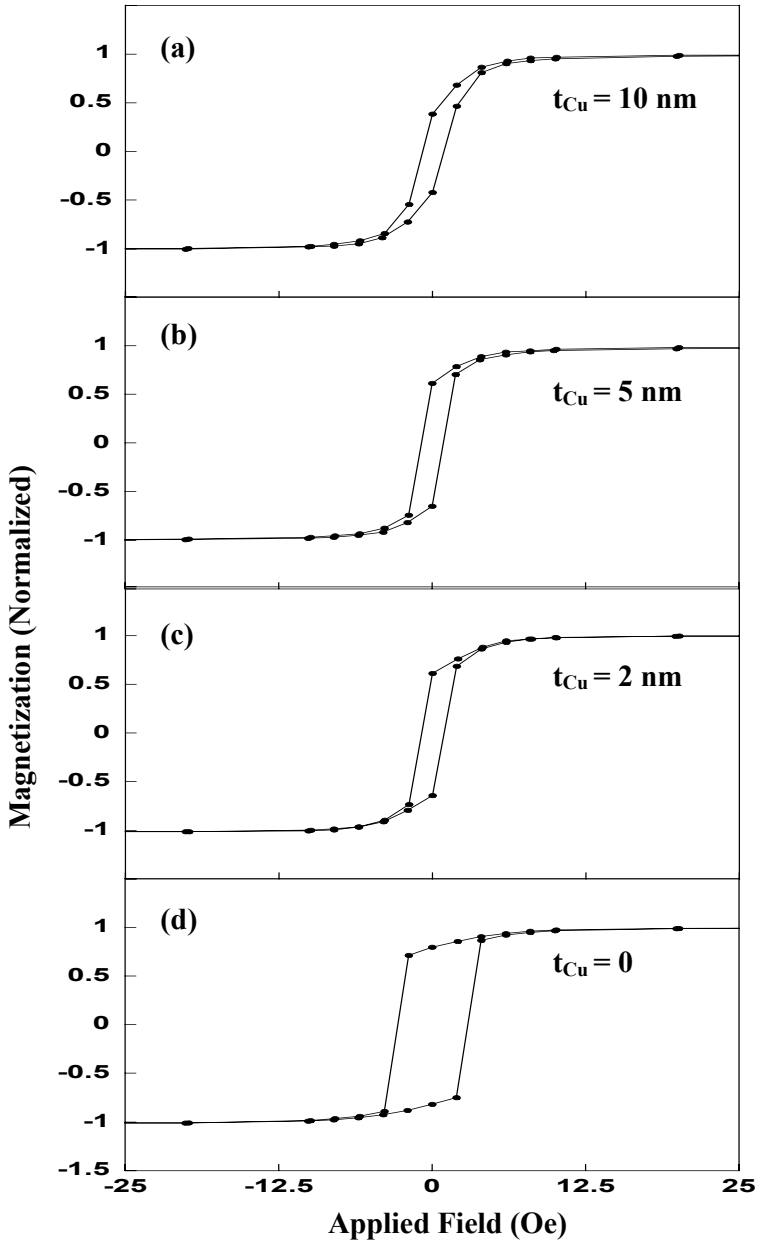


*Fig 5.9 Hysteresis loops as a function of Cu spacer layer thickness in [NiFe (10 nm)/ Cu ($t_{Cu}$)/ NiFe (10 nm)]$_2$ multilayer structure*

Shown in Fig (5.9) are the representative hysteresis loops measured on the reference [NiFe (10nm)/ Cu ($t_{Cu}$)/ NiFe (10 nm)]$_2$ films using VSM.

We observed a significant drop in the coercivity as the Cu interlayer is increased from zero. This is in contrast with the results obtained from [Co (10nm)/ Cu ($t_{Cu}$)/ Co (10 nm)]$_2$ multilayer films discussed in section 4.4. These results suggest that the exchange coupling mechanism is material dependent. The exchange length is also material dependent. From the M – H loops in Fig 5.9, material parameters such as coercivity, saturation field and squareness were extracted.

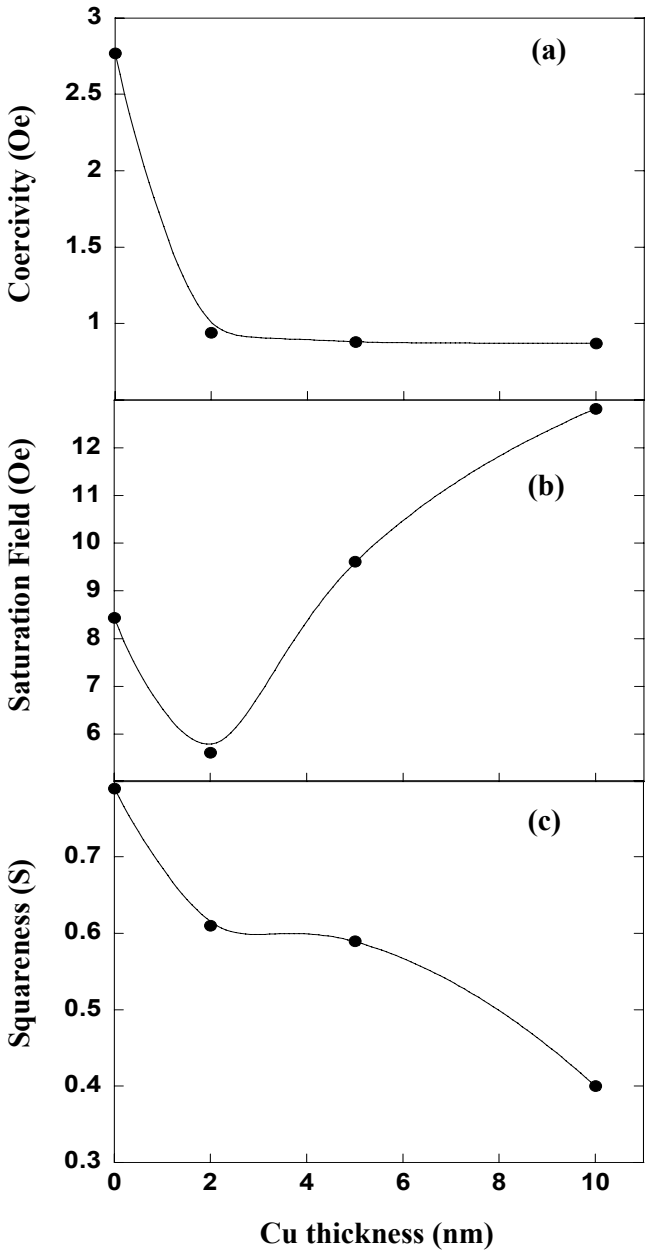


*Fig 5.10 The value of (a) coercivity ($H_c$), (b) saturation field ($H_s$) and (c) squareness as a function of Cu spacer layer thickness in [NiFe (10 nm)/Cu ($t_{Cu}$)/NiFe (10 nm)]$_2$ multilayer structure*

Shown in Fig 5.10 (a – c) are the coercivity ($H_c$), saturation field ($H_s$) and squareness (S) respectively. The coercivity dropped from (2.86 Oe) for $t_{Cu}$ = 0 to (0.9 Oe) for $t_{Cu}$ = 5 nm.

## 5. 5 Devices Fabricated using E - Beam Lithography Method

In this section, we present the experimental results for devices fabricated using e - beam lithography method. Using this method, the devices with very small width 500 nm and 1μm from [Co (10 nm)/Cu (2 nm)]$_2$ multilayer structure were made. The applied current was 100μA and the applied field was -1.5 kOe to 1.5 kOe. Fig (5.12) shows the comparison of PHE of the pattern size width (w = 1 μm) for different field orientations in the above structure.

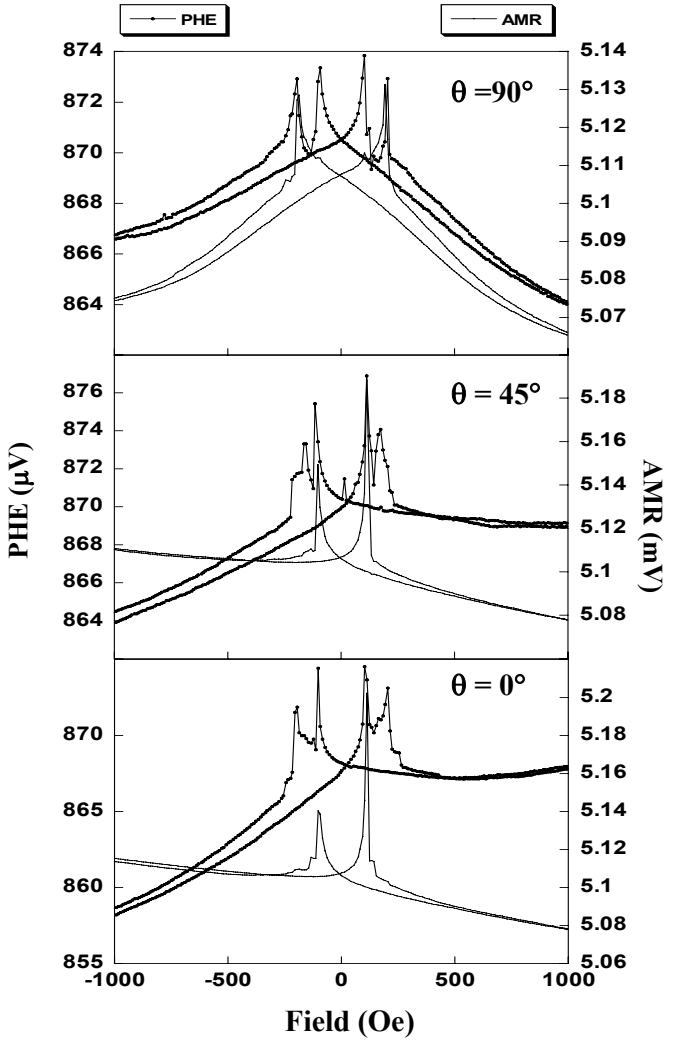


*Fig 5.11 Comparison of PHE and AMR output voltages for device width w = 1 μm*

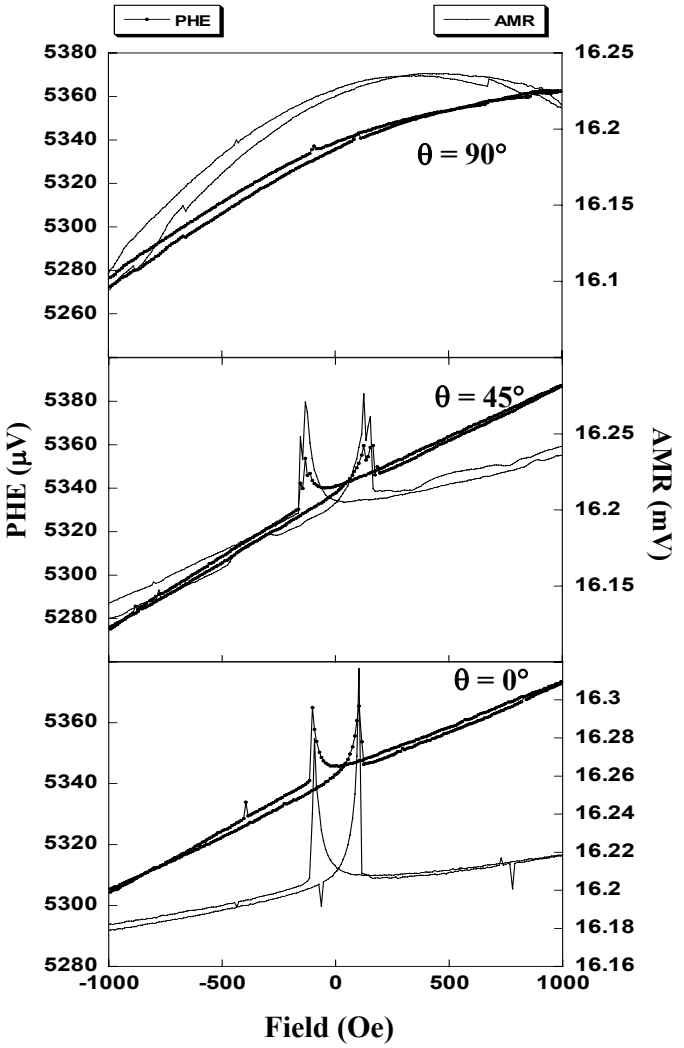


*Fig 5.12 Comparison of PHE and AMR output voltages for devices width w = 500 nm*

From Fig 5.11 and Fig 5.12, the PHE outputs are characterized by sharp jumps in both the forward and reverse field sweep. The exact origin of these peaks is unknown and further work be needed to confirm the origin.

## 5.6 Summary

We have investigated the role of finite size effect on the magnetic properties of multilayer films and the interlayer exchange coupling in [Co (10 nm)/ Cu ($t_{Cu}$)/Co (10 nm)]$_2$ and [NiFe (10 nm)/ Cu ($t_{Cu}$)/ NiFe (10 nm)]$_2$ structures. We observed that the results of PHE and AMR were very sensitive to the device width. Moreover, the switching field is also strongly dependent on the device width.

**Reference:**

[1] David Jiles, "Introduction to magnetism and magnetic materials", Chapman and Hall,"1991.

# Chapter 6

# Conclusion and Future Recommendations

## 6.1 Conclusion

In this project, the effect of Cu spacer layer thickness on the interlayer exchange coupling is investigated. The roles of finite size on the exchange coupling mechanism in Co/Cu and NiFe/Cu multilayer have been successfully investigated.

Initially, planar hall devices (PHE) were fabricated using shadow mask technique. Subsequently, PHE devices were fabricated by using optical and electron beam lithography techniques.

The effect of interlayer exchange coupling in [Co (10nm) /Cu ($t_{Cu}$)/Co (10nm)]$_2$ and [NiFe (10nm)/Cu ($t_{Cu}$)/ NiFe (10 nm)]$_2$ multilayers were investigated using a combination of planar Hall effects (PHE), anisotropic magnetoresistance measurements (AMR) and magnetic hysteresis. Sin2θ dependence on the PHE output was observed when the applied field (H) is greater than the switching field ($H_s$) of the device, in agreement with theoretical prediction. For fields $H<H_s$, a departure from the sin2θ dependent was observed due to domain wall propagation. From the comparison of AMR and PHE, we can conclude that PHE is sensitive to the magnetization direction in individual layers consisting the multilayers.

From our measurements, we observed that when the copper spacer layer thickness is less than 2 nm, ferromagnetic coupling is favored. For copper thickness greater than 2 nm, however, antiferromagnetic coupling dominated.

The results of PHE and AMR were very sensitive to the device width. In particular, the switching field is strongly dependent on the device width.

We can see clearly that the trend of coercivity, saturation field ($H_s$) and squareness as a function of Cu spacer layer thickness in [Co (10 nm)/ Cu ($t_{Cu}$)/ Co (10 nm)]$_2$ from evaporation technique and that from sputtering deposition technique are totally different. The magnetic properties (M – H loops) of the multilayer films deposited by different methods (sputtering method and evaporation) give a different trend in comparison.

## 6.2 Future Recommendations

Some recommendations for future work are:

1) Computer modeling of Planar Hall Effect should be done in the future.
2) In this project, we have fabricated and characterized the MR and PHE devices with both millimeter (mm) range and micronmeter (μm) range. Electron beam lithography method could be used to scale to nanometer (nm) range.
3) The exact origin of the peaks in [Co (10nm)/ Cu (5 nm)/ Co (10 nm)]$_2$ films by using e – beam method is unknown, therefore future work should be done to confirm the origin.
4) Other spacer layer materials such as Ta, Ru, Ag and Cr could be investigated using the same techniques in order to optimize the device performance.
5) Temperature dependence on the AMR and PHE should be investigated. At low temperature, impurity scattering is suppressed through interesting effect may be seen.
6) Some other characterization techniques like XRD should be performed to understand the correlation between the microstructure and magneto - electronic properties.